A synthetic morphogenic perceptory cell

Konstantin Gavriljuk[1,3], Farid Ghasemalizadeh[1,3], Bruno Scocozza[1,3], Akhilesh P. Nandan[1], Hans Seidel[1], Malte Schmick[1], Aneta Koseska[1], Philippe I. H. Bastiaens[1,2,4,*]

Affiliations

[1]Department of Systemic Cell Biology, Max Planck Institute for Molecular Physiology, 44227 Dortmund, Germany

[2]Faculty of Chemistry and Chemical Biology, TU Dortmund, 44227 Dortmund, Germany

[3]These authors contributed equally

[4]Lead Contact

*Correspondence: philippe.bastiaens@mpi-dortmund.mpg.de (P.B.)

SUMMARY

We reconstituted a Synthetic Morphogenic Perceptory System (SynMPS) by encapsulating a dynamic cytoskeletal microtubule (MT)-aster together with a light-actuated signaling system in a liposome. SynMPS responds to light with self-organized morphological state transitions that manifest as self-amplifying membrane deformations generated by the MT-aster recursively interacting with the signaling system. We demonstrate that the perception and response to external light pattern stimuli are shaped by prior exposures and the ensuing morphological states. The interdependence between cytoskeletal dynamics, membrane shape, and signaling thus generated a minimal out-of-equilibrium 'life-like' system that mimics context dependent morphological responses of cells to external cues.

Keywords

life-like synthetic cell, cellular shape changes, self-organization, signaling gradient, encapsulated microtubule asters, encapsulated signaling system, stigmergy

INTRODUCTION

Morphogenesis is an emergent property of living systems that maintain themselves in entropy dissipating non-equilibrium conditions (Prigogine and Nicolis, 1967; Schrödinger, 1944). This endows cells with the plasticity to generate forms in order to explore and recursively interact (Koseska and Bastiaens, 2017) with the outside world through the sensory signaling systems embedded in the plasma membrane. In this process, the outside information is mapped into an inner (cytoplasmic) biochemical state (Niethammer et al., 2007) that reflects the perception of the cell of the environment. We set out to reconstitute a minimal cell that can respond to environmental light cues by encapsulating a dynamic MT-aster cytoskeleton together with a membrane embedded signaling system. The signaling system consists of the MT-regulator stathmin whose phosphorylation is controlled by the light-induced translocation of AuroraB kinase (Sessa et al., 2005) on the membrane and freely diffusing λ-phosphatase (λ-PPase) (Zaytsev et al., 2016) in the liposome lumen. This signaling system thereby couples to cytoskeletal dynamics via a phospho-stathmin (pStathmin) gradient (Niethammer et al., 2004) that emanates from activated AuroraB on the membrane. The response of SynMPS to light is manifested as membrane extensions containing protruding microtubule bundles from the centrosomal aster. These in turn promote the activation of the signaling system, thereby recursively stabilizing SynMPS morphological states. We show that the interdependence between membrane shape and signaling (Schmick and Bastiaens, 2014) creates self-organized morphological states of SynMPS that can be altered by external light patterned templates. Such morphological responses can be described using a generalization of Pierre-Paul Grassé's concept of Stigmergy, which addresses the self-organized coalescence of sand grains into regular sand-pile structures by the collective behavior of social insects through indirect communication (Grassé, 1959).

RESULTS

The MT-aster-membrane cytoskeletal module

Following previous studies that reconstituted centrosomal or self-organized asters in water-in-oil droplets (Juniper et al., 2018; Laan et al., 2012; Pinot et al., 2009), we introduced self-assembled MT-asters in Giant Unilamellar lipid Vesicles (GUVs) by encapsulating purified centrosomes using cDICE (Abkarian et al., 2011) together with tubulin and GTP at concentrations where dynamic MT behavior occurs (Methods). To observe the asters in the GUVs by confocal laser scanning microscopy (CLSM), fluorescently labeled Alexa568-tubulin (~7.5 %) was also encapsulated. Since MT dynamics is a function of tubulin concentration (Figures S1A and S2B) (Mitchison and Kirschner, 1984), we imaged morphological states of GUVs containing low (20 μM) or high (35-40 μM) tubulin concentrations. Low concentrations resulted in a spherical morphology with a central positioning of a small MT-aster with minimal membrane deformations (Figures 1A and 1B). At high concentrations, extended MT growth led to peripheral aster positioning with strong membrane deformations (Figures 1A and 1B; Figure S1C). Two stable polar morphologies were observed with a peripheral centrosome and buckling MT-bundles that: 1) met at the other pole, or 2) generated membrane protrusion(s) at the opposite side. The convergence of the bending MTs into protrusions indicated self-induced capture sites (Schmick and Bastiaens, 2014). Short protrusions near the centrosome also

occurred. Decreasing the membrane tension by osmotic pressure facilitated creation of these self-induced capture sites (Figures 1A and 1B).

We concluded that fluctuating forces exerted on the centrosome by MT-bundles that interact with the membrane eventually position the centrosome at the periphery, generating the polar morphology. To observe this transition, an initial temperature of 20 °C was raised to 34 °C (Figure S1D). We monitored this for three proximal MT-GUV systems with different initial states (Figures 1C and 1D; Supplemental Video 1): single centrosome GUVs with high (a) and low (b) tubulin concentration and a GUV with 2 centrosomes (c). In (a), MT-bundles initially generated dynamic, radially distributed protrusions, due to transient interactions with the membrane, exerting a fluctuating force on the centrosome. This eventually led to peripheral centrosome positioning, with MT-bundles forming a stable protrusion at the opposite side. In contrast, the GUV with low tubulin (b) remained spherical and did not exhibit protrusions due to weak interactions of the short MT-aster with the membrane that moved the aster around (Figure S1E). Two opposed dynamic protrusions containing MTs from both centrosomes stabilized a bipolar morphology in (c). Tubulin eventually aggregated in the GUVs, likely caused by accumulated phototoxic damage (Video S1). Decreasing membrane tension prolonged the exploratory mode, enabling better observation of self-induced capture site dynamics (Figure S1F).

These dynamics were well recapitulated by a minimal agent-based model mimicking interaction of intrinsically dynamic MTs with a deformable boundary (Methods). The simulations showed metastable protrusions that eventually coalesced in a defined pattern in the absence of forces on the centrosome (Figure S1G; Supplemental Video 1). Implementing centrosome decentering led to two stable protrusions at opposite ends (Figure S1H; Video S2).

In order to affect MT-aster dynamics in the GUVs by biochemical activity, we first characterized the effect of the tubulin sequestering molecule stathmin (Curmi et al., 1994, 1997; Jourdain et al., 1997; Niethammer et al., 2004) on MT dynamics *in vitro*. Stathmin linearly decreased MT growth speed and abruptly increased catastrophe frequency (Figure S2A). In contrast, MT growth rate and catastrophe frequency were only weakly affected by pStathmin (Figure S2B) (Niethammer et al., 2004). These stathmin effects on MT dynamics strongly translated to MT-asters size (Figure S2C). We next encapsulated tubulin (40 μM) together with 5 μM stathmin or pStathmin and quantified the resulting morphological states (Figures 1E and 1F). With stathmin, small asters resulted in a spherical morphology, whereas with pStathmin the polar morphology was restored. These results show that MT-dynamics can be biochemically coupled to a kinase-based signaling system that affects stathmin phosphorylation.

The light-actuated signaling module

We developed a signaling module based on light-induced membrane translocation of AuroraB kinase, which phosphorylates stathmin (Gadea and Ruderman, 2006). For this, we introduced the iLID/SspB (improved Light-Induced Dimer/ Stringent starvation protein B) optical dimerizer system to GUV membranes (Figure 2A) (Guntas et al., 2015) by fusing iLID to a C2 lipid-binding domain (C2-iLID) that interacts with phosphatidylserine. Up to 2 pmol/cm² of SspB was reversibly and homogeneously recruited to the membrane upon blue light (458/488 nm) stimulation (K_D = 360 ± 60 nM, Figure S3A). Similar recruitment densities and kinetics were obtained for light-induced recruitment of fluorescent Alexa488-SspB-AuroraB/INCENP$_{in\text{-}box}$

(SspB-AuroraB) in presence of 1 μM soluble λ-PPase, which is known to dephosphorylate $INCENP_{in\text{-}box}$ (Inner centromere protein A, amino acids 834 – 902) (Zaytsev et al., 2016) (Figure 2B; Figures S3B and S3C). In this case however, regular patterns of SspB-AuroraB clusters were formed on the outside of GUVs upon continuous blue light illumination, irrespective of ATP in the system (Figures 2C and 2D top; Figure S4A). These regular patterns exhibited three main harmonic frequencies (Figure 2E; Figure S4B), which were lost upon lowering the light energy by a factor of ~6 (Figures 2D bottom and 2E; Figures S4A and S4B). This shows that SspB-AuroraB patterning requires light-induced cycling of monomers to the membrane. Furthermore, in the absence of light, SspB-AuroraB monomers rapidly dissociated from the membrane, whereas clusters persisted (Figure S4C). Inside GUVs, the same phenomenon of SspB-AuroraB patterning occurred upon light-induced translocation, albeit with smaller clusters (Figure 2C; Video S3). This is most likely due to the limiting SspB-AuroraB amount in the GUV. These observations show that SspB-AuroraB cluster patterning emerges from a light-energy driven self-organizing process based on substrate depletion (or analogous C2-iLID binding site saturation) and cooperative cluster formation. In these clusters, ATP-driven autocatalytic activation of SspB-AuroraB by trans-phosphorylation occurs (Noujaim et al., 2014; Sessa et al., 2005), whereas dissociating monomers get inactivated by λ-PPase activity in the lumen of the GUV.

We next coupled light-induced SspB-AuroraB activity to MT-aster dynamics by introducing stathmin in the system, where the freely diffusing λ-PPase in the lumen can generate a pStathmin gradient (Niethammer et al., 2004) that emanates from activated SspB-AuroraB clusters. This localized phosphorylation cycle that releases tubulin from stathmin in the vicinity of SspB-AuroraB clusters constitutes an ATP-driven molecular 'pump' that enhances local tubulin concentration near the membrane (Figure 3A). This tubulin concentration gradient near the membrane can thereby locally promote MT-polymerization. We derived optimal conditions for this tubulin gradient using reaction-diffusion simulations (Methods) with measured kinetic parameters. To obtain the kinetic parameters of stathmin phosphorylation (Table S1), we developed an organic dye containing variant of the stathmin FRET sensor COPY (Niethammer et al., 2004) (Atto532-stathmin-Atto655: $COPY^{o}$ (organic)), which reports the conformational transition upon binding of tubulin to dephosphorylated stathmin (Figures 3A and 3B; Figures S5A and S5B). This can be determined either by the fluorescence ratio of Atto655/Atto532 or by the change in fluorescence lifetime of the donor Atto532 (Methods). From the kinetics of $COPY^{o}$ phosphorylation/dephosphorylation in solution (Figure S5C; Table S1), we derived that only ~5% of stathmin is phosphorylated in solution for equal concentrations of 1 μM SspB-AuroraB and λ-PPase. Light-induced recruitment of SspB-AuroraB to the membrane increases its concentration by at least a factor of 500 (Methods), which locally increases the fraction of pStathmin to >96%. The shape of the pStathmin gradient depends on the interplay of λ-PPase activity, diffusion, and association/dissociation kinetics of stathmin-tubulin. We therefore also determined stathmin-tubulin association/dissociation kinetics (Figure S5D; Table S1). A high and a low affinity binding site for α,β-tubulin dimers (30 ± 3 nM, 2.00 ± 0.02 μM, respectively) were identified, where only high affinity binding was abolished upon phosphorylation. Using these parameters, the simulation revealed that kinase activity only affects gradient amplitude, whereas λ-PPase activity determines both decay length as well as amplitude (Figure 3C; Figure S5E). A total activity of λ-PPase of ~0.01 s^{-1} (~1 μM) generated an optimal tubulin gradient with

a ~0.5 μm decay length, which coincided with the pStathmin gradient and was robust to changes in λ-PPase concentration over an order of magnitude.

The tubulin gradient was next measured ratiometrically with COPY^{o} on the outside of GUVs functionalized with iLID via a prenyl lipid anchor (iLID_G, Methods) in order to reach high densities of SspB-AuroraB recruitment. Steep (~0.5 μm) gradients emanated from the membrane in the presence of 250 nM or 4.5 μM λ-PPase upon light-induced recruitment of SspB-AuroraB that were not observed in the absence of λ-PPase (Figures 3D–3F). To now measure the tubulin gradient inside GUVs, we encapsulated 12 μM SspB-AuroraB, 5 μM C2-iLID, 6 μM COPY^{o}, 1 μM λ-PPase and 2 mM ATP (Figure 3G; Figure S3D). In the absence of λ-PPase, COPY^{o} reported a fully phosphorylated state, whereas with λ-PPase COPY^{o} was maintained in a dephosphorylated steady-state. Upon recruitment of SspB-AuroraB, tubulin gradients emanated from the membrane, which were absent without the λ-PPase (Figures 3H and 3I; Figure S6). These gradients emerged from patterned structures, most likely reflecting the spatially organized clusters of active SspB-AuroraB. We next investigated whether encapsulation of this signaling with the cytoskeletal module enables light-induced signaling control of MT-dynamics and thereby GUV morphology.

Integrating the signaling and cytoskeletal modules inside GUVs

GUVs in which both the cytoskeletal and signaling module were encapsulated (referred to as SynMPS) manifested three morphological types (Figure 4A; Figure S7). The spherical and polar morphologies correspond to the low and high tubulin cases observed in the absence of the signaling module (Figure 1A). A new star-like morphology was also observed, indicating that membrane deformation by MTs can actuate signaling in the absence of light, thereby generating membrane protrusions at much lower MT-bundle densities. To investigate this reverse causality, we encapsulated both modules in the absence of stathmin (SynMPS^{-stat}). After light-induced translocation, enhanced density of SspB-AuroraB in MT-bundle protrusions showed that AuroraB is preferentially recruited to strongly deformed membrane surfaces (Figure 4B). This is likely caused by increased membrane surface to 'cytoplasmic' volume ratio in concave membrane deformations (Rangamani et al., 2013; Schmick and Bastiaens, 2014). The increased SspB-AuroraB density on the membrane further enhances its self-association and thereby augments local kinase activity. Membrane deformation by protruding MT-bundles thus actuates SspB-AuroraB, thereby enabling recursive interactions between the cytoskeletal and signaling module in the presence of stathmin (Figure 4C).

To investigate if SynMPS generates protrusions in response to light illumination, tubulin and SspB-AuroraB were imaged at the equatorial plane by CLSM before and during global light activation in both a SynMPS and SynMPS^{-stat} with spherical morphology (Figure 4D; Video S4). Radial membrane deformations were quantified as a function of time (Figure 4E) and related to the corresponding distribution of SspB-AuroraB fluorescence in merged kymographs (Figures 4F and 4G). Upon translocation of SspB-AuroraB in SynMPS^{-stat}, fluorescence speckles of SspB-AuroraB around the membrane indicated transient micro-protrusions caused by dynamically instable astral MTs weakly interacting with the membrane. This SynMPS^{-stat} maintained the spherical morphology (Figures 4D upper panel, 4E and 4G left kymograph). In contrast, SynMPS responded to blue light with radially distributed strongly bending protrusions that recruited SspB-AuroraB and appeared in clusters (Figures 4D lower panel and 4G right

kymograph). As opposed to the protrusions generated in the absence of the signaling module (Figure 1A), these protrusions often sprouted two or more sub-branches (Figure 4D lower panel enlargements). The sprouting protrusions indicated that local activation of the stathmin mediated tubulin 'pump' by SspB-AuroraB accelerates MT polymerization, such that individual MTs of a bundle can locally deform the membrane. The enhanced tubulin gradients in the protrusions can in turn feed back into MT polymerization, generating a self-amplified structure (Figure 4C). The stabilization of MT-bundles in these protrusions reinforces a centrally positioned aster together with isotropically distributed protrusion clusters (Figure 4H).

To investigate if these protrusions can be organized towards an external stimulus, we locally activated SspB-AuroraB by continuously irradiating a Localized Region (irLR) of SynMPS with blue light. This resulted in a gradient of activated SspB-AuroraB that emanates from the light-activated SynMPS surface due to its diffusion along the membrane and dissociation in the dark areas (Figure 5A left panel). Similar to global activation, light-induced translocation of SspB-AuroraB in SynMPS^{-stat} had no effect on its spherical morphology, and transient fluorescence speckles of SspB-AuroraB occurred rarely in the irLR (Figure 5A middle and right panels). However, a star-like SynMPS that was continuously irradiated in the upper right area immediately responded in the irLR with membrane protrusions containing high levels of SspB-AuroraB (Figures 5B–5D; Video S5). These protrusions were clearly caused by astral MT-bundles (Figure 5B arrows), and sprouting was also observed in the irLR (Figure 5B upper panel enlargements). During the course of irradiation, a light-induced morphing process was apparent (Figures 5B lower panel and 5C), starting from star-like, through spherical and ending in a polar morphology that was oriented towards the irLR. The disappearance and genesis of protrusions that collectively dictate centrosome position and shape of SynMPS (Figures 5C and 5D) thereby indicated that an external light stimulus template evokes a transition between dynamically maintained self-organized morphological states (Figure 5E; Video S6; Figures S8A–S8C).

To investigate how the response of SynMPS depends on its stimuli history and initial state, we transiently irradiated several areas in sequence and measured the resulting morphological state transitions (Figure 6). Starting from a polar SynMPS with two protrusions, one proximal to the centrosome and a protrusion cluster at the opposite end (Figure 6C left), irradiation in the right area triggered the formation of a new protrusion in the irLR that persisted after light removal (Figures 6A and 6B; Video S7). This genesis correlated with the loss of the clustered protrusion. Subsequent irradiation in the upper left area also induced the formation of protrusions, of which at least one was persistent after irradiation stopped. Equivalent protrusion genesis that correlated with the loss of the main protrusion was observed upon a third irradiation in the lower right area (Figure 6B). This sequence of local stimulations therefore resulted in the formation and disappearance of protrusions and a transition to a spherical morphology that was unaltered by global irradiation at the end (Figure 6C right; Video S8). We also irradiated the left and right areas with respect to the major axis of a star-like/polar SynMPS, with a pronounced protrusion opposite to the centrosome and three proximal ones. Protrusions were generated in both irLRs that were generally attracted to the main protrusion, further stabilizing it (Figures 6D and 6E; Video S9). This resulted in a morphological transition in which the three centrosome-proximal protrusions converted to a polar membrane deformation, and two protrusions flanking the main one appeared. This light-induced morphological transition was therefore constrained by the main-axis protrusion (Figure 6F; Video S10). In contrast, a polar SynMPS with a weaker main-axis protrusion responded to a sequence of flanking irradiations with a transition to a spherical

morphology (Figures S8E–S8F). These experiments thereby show that the morphogenic plasticity of SynMPS is dependent on its initial state and stimuli history.

DISCUSSION

Grassé's stigmergic concept of collective behavior of social insects through indirect communication (Grassé, 1959) paraphrases how fluctuations around uniformly distributed density of matter can generate stable self-amplifying structures in a self-organizing manner by leaving a sign (stigma) on work (ergon) in progress (Figure 7A). The fundamental principle of local matter coalescence through self-amplification, which in turn depletes the substrate from the surrounding represents a minimal model through which stigmergy can be realized, and can therefore exemplify a large class of systems (Deneubourg, 1977; Susnea and Axenie, 2015; Tabony, 2006; Theraulaz et al., 2003). Bringing it to the molecular systems relevant to SynMPS, both the light-driven SspB-AuroraB clustering on the membrane, as well as the self-induced capture sites of membrane protrusions (Schmick and Bastiaens, 2014) are stigmergic (Figures 7B and 7C). In the former case, the SspB-AuroraB clusters are dynamically maintained due to light-energy driven matter exchange between the clusters and the free monomers in the cytoplasm. Dynamically equivalent cellular systems are nucleotide cycling systems such as GTPases that convert chemical (GTP/GDP) energy to recruit and thereby deplete effector proteins from the cytoplasm to the membrane of a cell (Schmick and Bastiaens, 2014) where they cooperatively form clusters. In the latter case, the deformations resulting from the interactions of the dynamically instable cytoskeletal MT-aster with the plasma membrane will capture more neighboring astral microtubules, thereby generating self-induced capture sites that deplete radially distributed MTs. We formalized the concept of stigmergy in a paradigmatic reaction-diffusion model where self-amplification of local structures triggers depletion of its free substrate. This leads to a symmetry breaking transcritical bifurcation at a critical total substrate concentration (Figure 7D): above it, spatial-temporal structures emerge from initially uniform substrate distribution (Figure 7E top and middle). An environmental spatial-temporal signal such as the extracellular light gradient in SynMPS (Figure 5A) imposed an external template that constrained the self-organized solutions of the system (Bastiaens et al., 2006; Raspopovic et al., 2014; Theraulaz et al., 2003), resulting in regular structures oriented by the template (Figure 7E bottom).

The encapsulated fuel in the form of ATP and GTP chemical potential established the non-equilibrium conditions, necessary for generating self-organized SynMPS morphological states. The interdependence between cytoskeletal dynamics, membrane shape, and signaling resulted in perceptory SynMPS morphogenic responses, where perception stands not only for the passive receipt of signals, but for the ensuing response that is shaped by the internal state resulting from prior exposures. The light-induced transitions between morphological states are thereby triggered by changes of the substrate bifurcation parameter in the signaling module (Figure 7D). Much has to be learned from SynMPS on the structural stability of the emergent morphological states (Thom, 1994) that are a direct consequence of the attractors of the system, as well as on its plasticity and reversibility in response to external stimuli. For example, since membrane deformation by MT-bundles actuate signaling, we also expect that morphological state transitions in SynMPS can be triggered by externally imposed mechanical stimuli that deform the membrane.

The short lifespan of SynMPS is constrained by the encapsulated fuel store (ATP, GTP) and the stability of the proteins. The latter can be improved by encapsulating protein stabilizing agents as well as radical scavengers. On the other hand, by reconstitution of an artificial photosynthetic membrane (Steinberg-Yfrach et al., 1998), SynMPS could convert light energy into ATP or even GTP chemical potential that could maintain its non-equilibrium state over prolonged periods.

Maturana and Varela proposed that autopoiesis and cognition define the realization of the living (Maturana and Varela, 1980). The intrinsic self-organizing dynamics of recursively interacting SynMPSs has the potential to cognitively (Koseska and Bastiaens, 2017) generate new morphologies that differ from the single synthetic systems. In this study, we imposed the extracellular light signals that SynMPS perceives and therefore the next step is to have several SynMPS recursively communicate among each other. Autopoiesis on the other hand, refers to the process through which a system can replicate its own components. This will be much harder to achieve, but recent progress in generating self-replicating DNA by its encoded proteins in liposome-based synthetic cells (van Nies et al., 2018) as well as reconstitution of bacterial cell division (Litschel et al., 2018) would in principle allow the generation of a replicating SynMPS.

ACKNOWLEDGMENTS

The authors thank Peter Bieling for reagents and helpful discussions, Roger Goody for assistance with the stopped-flow experiments, H. Schütz, M. Reichl, and S. Gentz for technical assistance and A. Krämer for critical reading of the manuscript. This project was funded by the BMBF/MPG network MaxSynBio (031A359A).

AUTHOR CONTRIBUTIONS

K.G. generally developed biochemical assays as well as COPY^{o}, purified and encapsulated proteins, performed biochemical and imaging experiments. F.G. generated encapsulated asters, performed MT assays and imaging experiments, B.S. developed image and morphometric analysis with help of P.B. and performed image quantification, A.N. performed numerical simulations, H.S. performed biochemical assays and imaging experiments, M.S. performed the gradient reaction-diffusion simulations, A.K. & P.B. developed theoretical concepts, A.K. performed bifurcation analysis, P.B. conceived and supervised the project and wrote the manuscript with help of K.G. and A.K.

DECLARATION OF INTERESTS

The authors declare no competing interests.

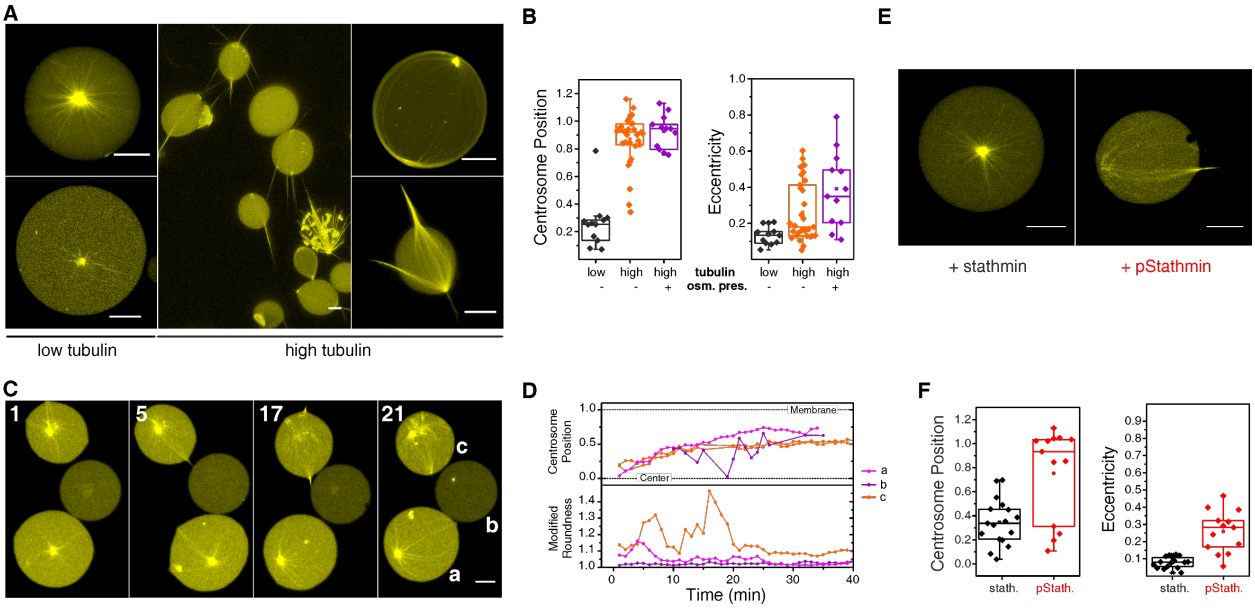

Figure 1. Morphological states of encapsulated MT-asters

(A) Morphologies of GUVs generated at low (20 µM) or high (35-40 µM) tubulin concentration. Central image: GUVs with decreased membrane tension. (B) Morphometric quantification (centrosome position (left) and eccentricity (right)) of GUVs with low or high tubulin concentration as well as for GUVs with increased external osmolarity. Centrosome position: 0 – centered, 1 – membrane proximal, eccentricity: 0 – perfect circle, >0 – deviations from circle. Each dot corresponds to a separate GUV. (C) CLSM time-lapse of temperature induced morphological state transitions of encapsulated asters (numbers indicate time in min). a-c correspond to three different GUV morphologies (see text). (D) Centrosome positions (top) and modified roundness (bottom) for GUVs in (C). Modified roundness: 1 – perfect circle, >1 – deformation. Missing positions: centrosome out of focal plane. (E) Representative images demonstrating the effect of stathmin (5 µM, left) or pStathmin (5 µM, right) on the morphology of encapsulated MT-asters (40 µM tubulin). (F) Corresponding morphometric quantification of multiple GUVs. Scale bars 10 µm.

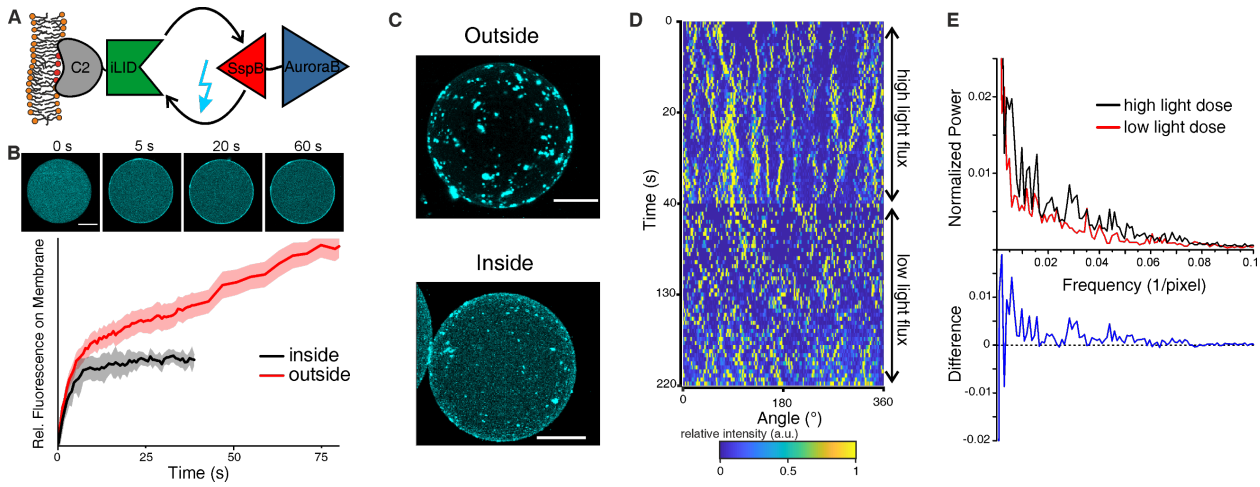

Figure 2. Light-induced SspB-AuroraB recruitment on GUV membranes

(A) Scheme of light-induced signaling system. C2 (grey), iLID (green), SspB (red), kinase domain of AuroraB (blue), blue arrow indicates light-induced interaction. (B) SspB-AuroraB membrane translocation. Examples show translocation inside GUVs (5 µM C2-iLID, 12 µM SspB-AuroraB). Bottom graph: light-induced translocation kinetics outside (red) and inside (black) (mean ± SD, N = 7 – 9 for each case). (C) Exemplary maximum intensity projections of confocal z-stacks of Alexa488-SspB-AuroraB fluorescence viewed from top (top: recruitment outside, bottom: recruitment inside) acquired after 5 min of blue light illumination including the acquisition of the z-stack (Video S3). (D) Representative angular intensity distribution kymographs of Alexa488-SspB-AuroraB fluorescence at the equatorial membrane recruited to the outside of GUVs for high and low blue light energy fluxes. Sampling rate was 6x larger for first activation series (high light flux, until 40 s) than the second (low light flux, 40 – 220 s). Samples contained 1 µM λ-PPase. (E) Normalized power spectra of time-integrated kymographs for high (black) and low (red) light flux. Top: geometrical average spectrum of 7 GUVs, bottom: difference spectrum (high – low light dose). Additional traces and spectra in Figure S4.

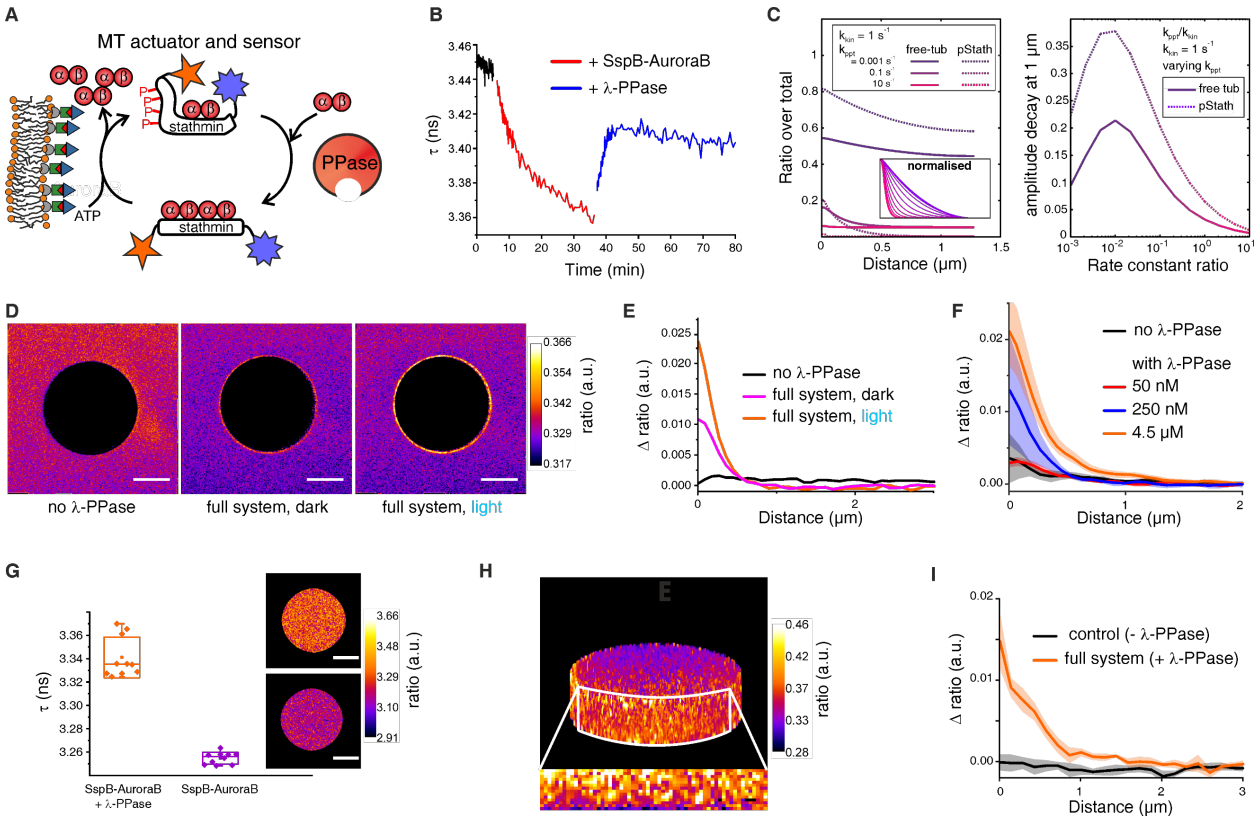

Figure 3. Tubulin gradient

(A) Scheme of stathmin phosphorylation cycle releasing tubulin at the membrane. C2-iLID/SspB-AuroraB on the membrane as in Figure 2A. α,β: tubulin heterodimers, PPase: λ-phosphatase, conjugated Atto532 (orange) and Atto655 (violet) turn stathmin into COPY^{o}. (B) Fluorescence lifetime (τ) measurement of COPY^{o} phosphorylation and dephosphorylation in bulk (10 μM COPY^{o}, 20 μM tubulin, 2 μM SspB-AuroraB, 500 nM λ-PPase). (C) 1D-simulation of tubulin gradient generated by stathmin phosphorylation cycle (kinetic parameters in Methods). Left panel: free tubulin (solid lines), free pStathmin fraction (dashed lines). Gradient decay lengths (inset, left panel) and amplitudes (right panel) for different PPase activity. k_{kin}: phosphorylation reaction rate, k_{ppt}: dephosphorylation reaction rate. (D) Ratiometric images of COPY^{o} outside of GUVs with iLID_G on the membrane, SspB-AuroraB and tubulin in the bulk (concentrations in Methods). Left: without λ-PPase. Center: 250 nM λ-PPase in the dark. Right: after light-induced translocation of SspB-AuroraB. (E) Quantification of (D). (F) Quantification of gradients with different λ-PPase concentrations (mean ± S.E.M. of 4 GUVs for each condition). (G) COPY^{o} fluorescence lifetimes (τ) in GUVs with full signaling system (orange, Methods) or without λ-PPase (purple). Example images to the right. (H) COPY^{o} phosphorylation gradient in a GUV: Maximum intensity projection of 8-slice ratiometric z-stack and 2D map of GUV surface. (I) Quantification of multiple GUVs as in (H) (control: mean ± S.E.M. of 6 GUVs, full system: mean ± S.E.M. of 4 GUVs). Scale bars 10 μm.

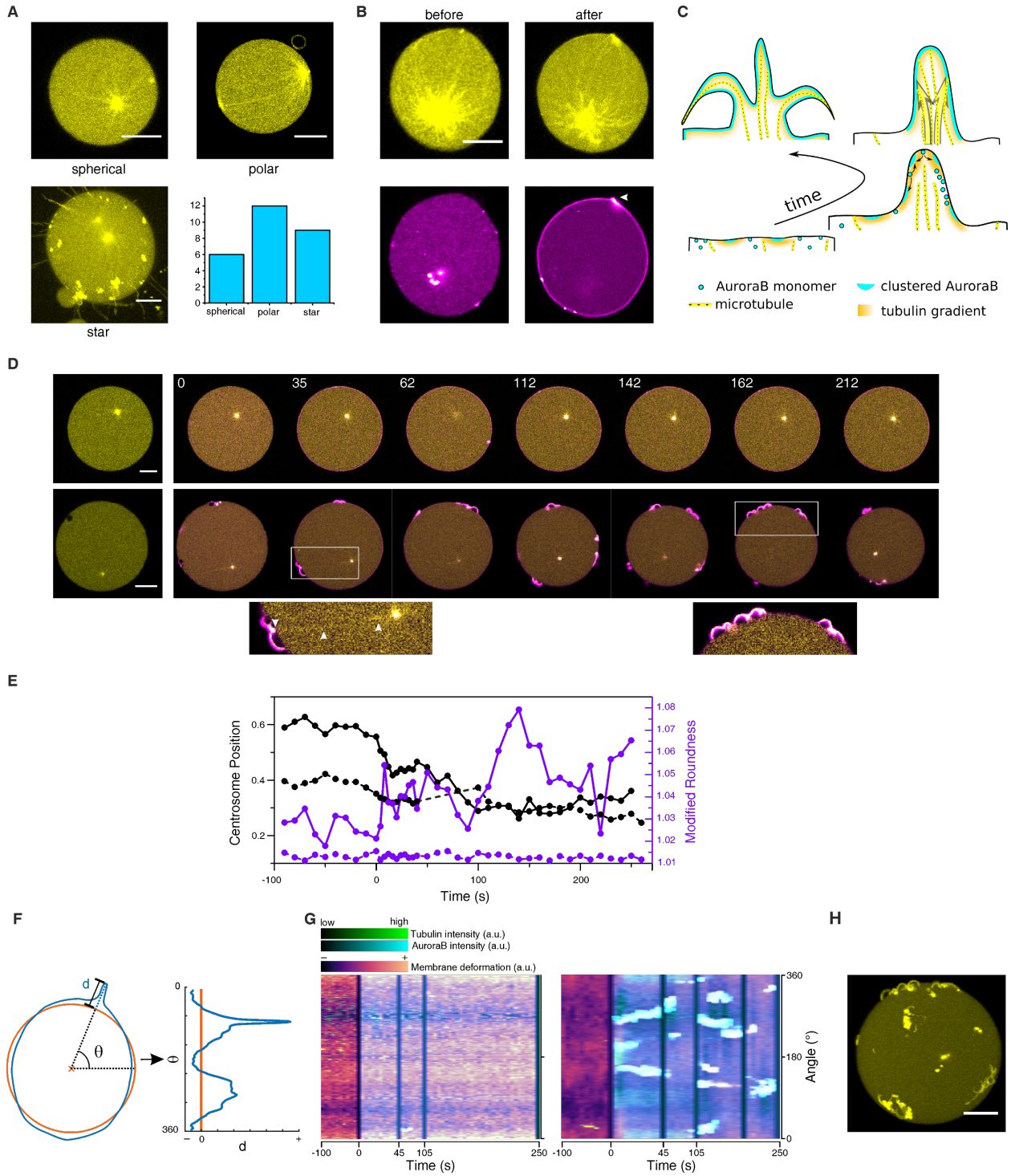

Figure 4. SynMPS response to global light activation

(A) Representative images and quantification of SynMPS morphologies (See also Figure S7). (B) CLSM images of Alexa647-tubulin (yellow) and Alexa488-SspB-AuroraB (magenta) in a polar SynMPS^{-stath} before (left panels) and after ~4 min of continuous blue light irradiation (right). Arrow indicates protrusion. (C) Scheme of protrusion genesis. See legend for components. (D) CLSM time lapse of Alexa647-tubulin (yellow) and Alexa488-SspB-AuroraB

(magenta) at the equatorial plane of spherical SynMPS^{-stath} (upper panels) and SynMPS (lower panels) prior to (first column) and during continuous global illumination with blue light. Numbers in panels indicate measurement time in seconds (Video S4). Enlargement of white rectangles shown below. Arrow heads point to MT bundle that generates a sprouting protrusion. (E) Time-courses of centrosome positions (black) and modified roundness (purple) for SynMPS^{-stath} (dashed lines) and SynMPS (solid lines). (F) Scheme of mapping distribution of radial membrane deformations into linear kymographs. d is the distance to the best fit circle of the GUV shape and is a measure of membrane deformation (positive when membrane is outside of circle, negative when inside), and θ the angle along the circle (Methods). (G) Overlaid kymographs of membrane deformation (magma), Alexa647-tubulin (green) and Alexa488-SspB-AuroraB (cyan) fluorescence distribution along the membrane. Negative time: prior to activation. Vertical lines are short interruptions in the measurement. Left: SynMPS^{-stath}, right: SynMPS. (H) Maximum intensity projection of Alexa647-tubulin fluorescence of a confocal z-stack obtained after the time lapse series of SynMPS. Scale bars 10 µm.

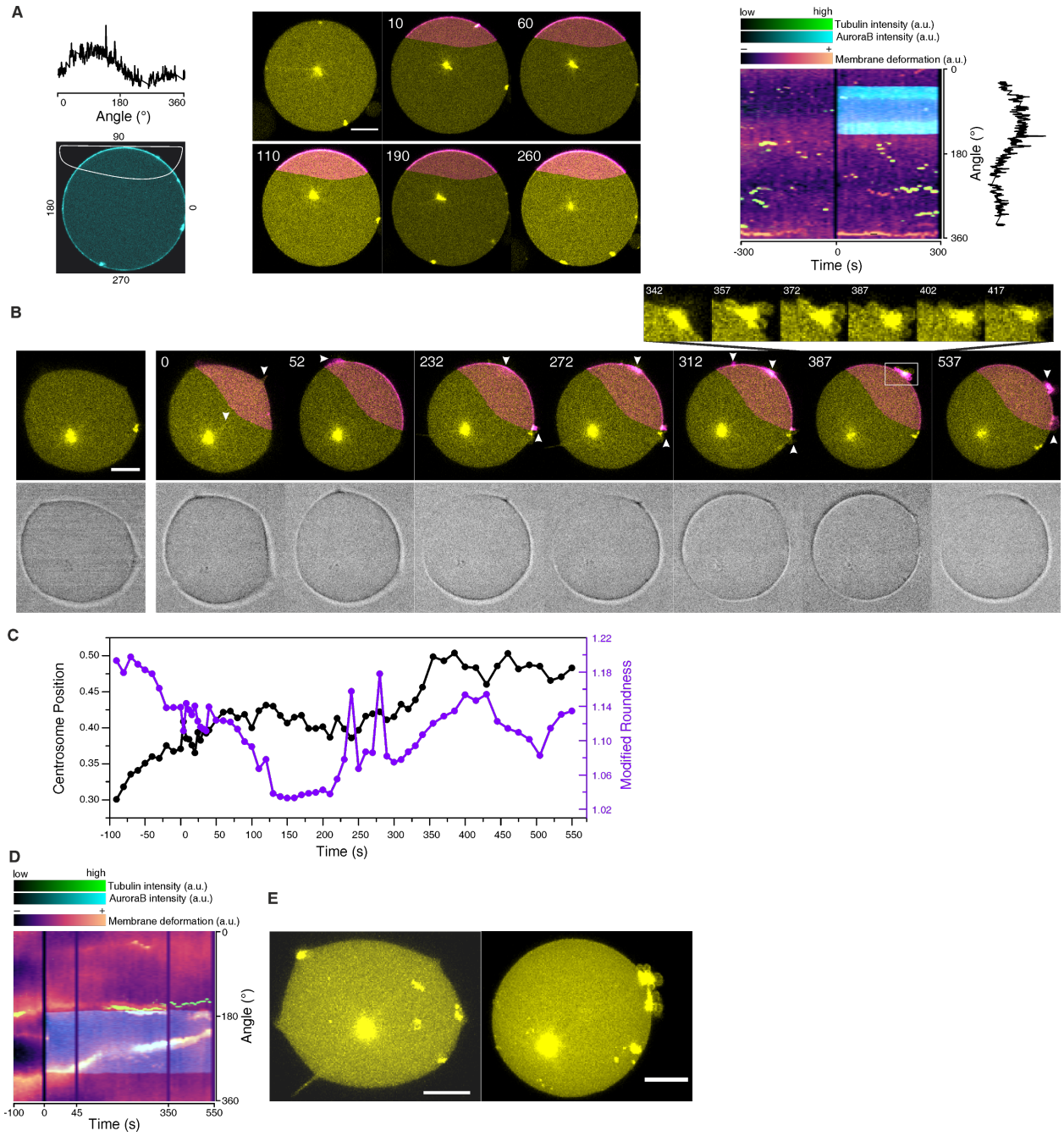

Figure 5. SynMPS response to local light activation

(A) Left panel: SspB-AuroraB activation gradient resulting from continuous blue light irradiation of a localized region (irLR, enclosed by white lines) in SynMPS^{-stath}. Middle panels: Selected micrographs of CLSM time lapse of Alexa647-tubulin (yellow) and Alexa488-SspB-AuroraB (magenta) fluorescence at the equatorial plane of spherical SynMPS^{-stath} prior to (first image) and during continuous local illumination with blue light. Numbers in panels indicate measurement time in seconds. Right panel: corresponding overlaid kymographs (as in Figure 4) with gradient profile on the side. Negative time: prior to activation. Vertical lines indicate short interruptions in the measurement. (B) CLSM time lapse of Alexa647-tubulin (yellow) and Alexa488-SspB-

AuroraB (magenta) fluorescence (upper panels) and transmission (lower panels) of star-like SynMPS prior to (first column) and during continuous local illumination with blue light (Video S5). Increased time resolution sequence of area bounded by white rectangle shown above. Arrows indicate protrusions. (C) Time-courses of centrosome positions (black) and modified roundness (purple) for SynMPS in (B). (D) Corresponding overlaid kymographs. (E) Maximum intensity projections of Alexa647-tubulin fluorescence of a confocal z-stack obtained before (left) and after (right) the time lapse series (Video S6). Scale bars 10 µm.

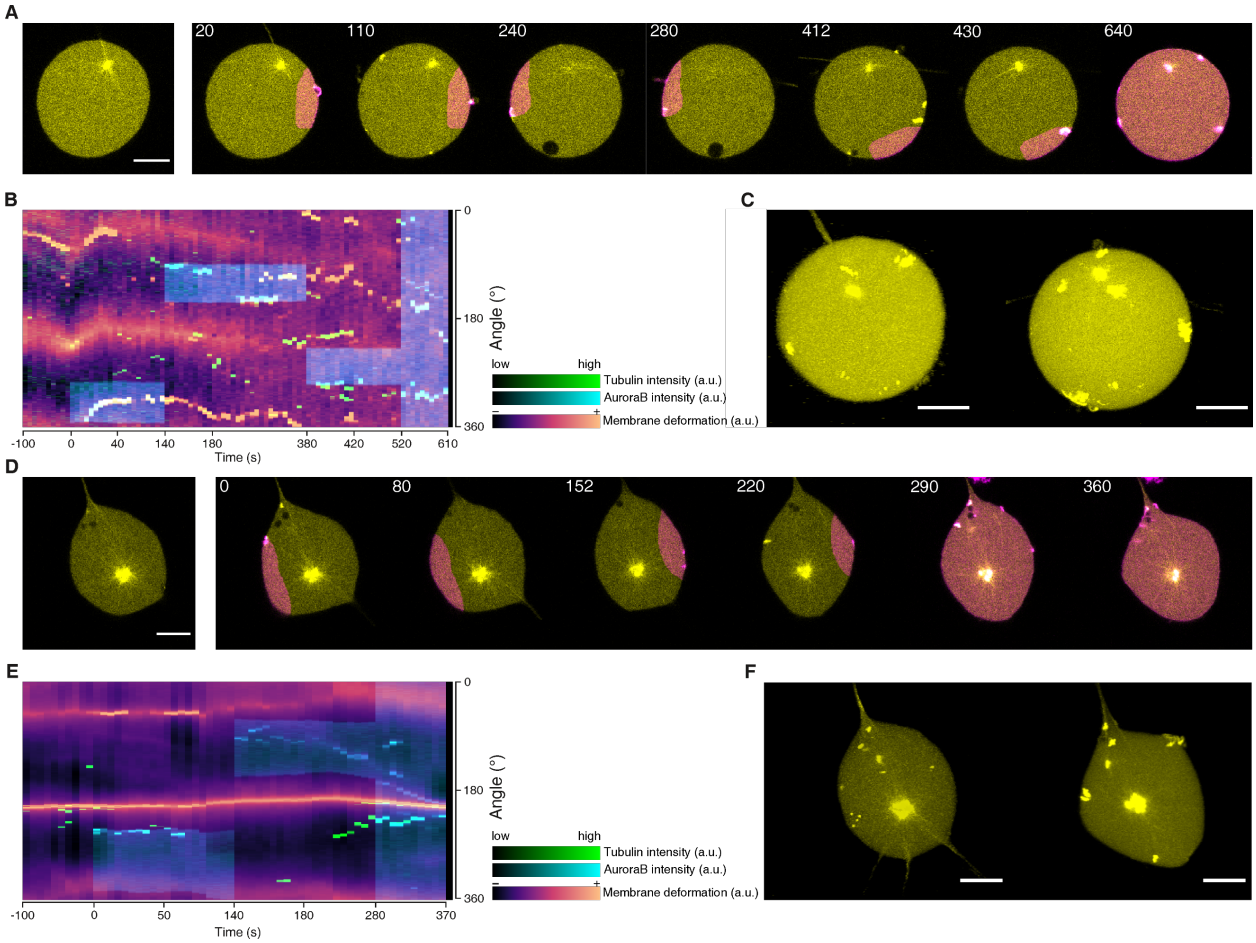

Figure 6. SynMPS response to sequential activation in different areas

(A) CLSM time lapse of Alexa647-tubulin (yellow) and Alexa488-SspB-AuroraB (magenta) fluorescence of a polar SynMPS prior to (first column) and during sequential transient local illumination with blue light in different areas. Numbers in panels indicate measurement time in seconds. Arrows indicate protrusions. (B) Corresponding overlaid kymographs. Negative time: prior to activation. (C) Maximum intensity projections of Alexa647-tubulin fluorescence of a confocal z-stack obtained before (left) and after (right) time lapse series (arrow indicates clustered protrusion). (D) CLSM time lapse (as in (A)) of a star-like/polar SynMPS. Arrows indicate protrusions. (E) Corresponding overlaid kymographs and (F) maximum intensity projections obtained before (left) and after (right) the time lapse series.

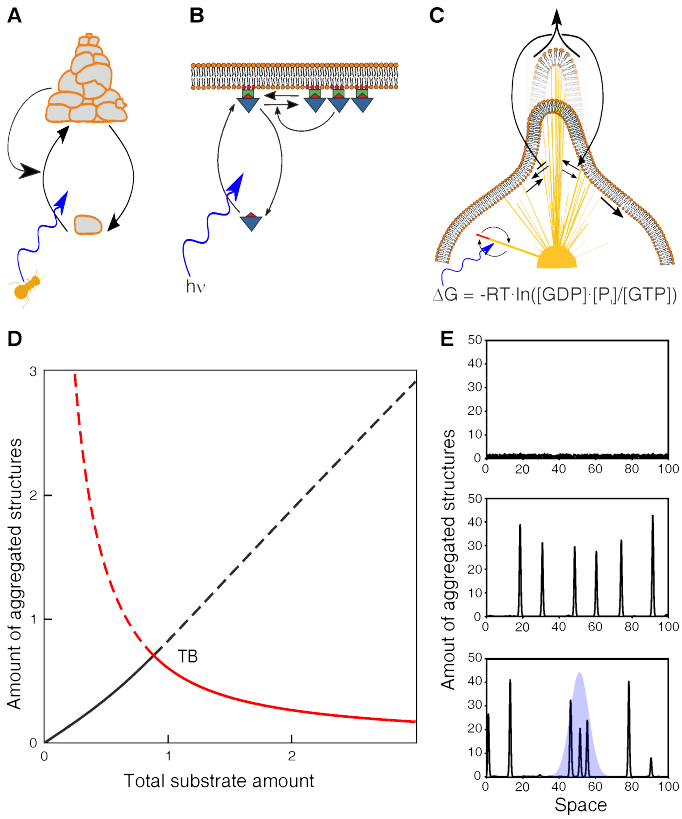

Figure 7. Dynamic features of stigmergy

Schematics of stigmergic mechanisms depicting (A) Termite-mediated building of self-amplified sand pillars coupled to depletion of free sand grains; (B) Cooperative protein cluster formation on a membrane due to depletion of cytoplasmic substrate through light energy (hν) driven recruitment, and (C) Stigmergic membrane deformations generated by self-induced capture sites of dynamic microtubules. ΔG: GTP/GDP·P_i Gibbs free energy. (D) Bifurcation diagram of a generalized substrate-depletion model for A-C, depicting symmetry breaking at a critical total substrate amount. Solid lines denote stable solutions: black – homogenous steady state, red – inhomogeneous state; dashed lines – unstable solutions; TB – transcritical bifurcation. (E) Starting from uniform steady state (top), pattern formation arises from substrate diffusion in one dimension (middle). An external gradient template (blue shaded area) orients the pattern (bottom). Equations and parameters in Methods.

REFERENCES

Abkarian, M., Loiseau, E., and Massiera, G. (2011). Continuous droplet interface crossing encapsulation (cDICE) for high throughput monodisperse vesicle design. Soft Matter *7*, 4610.

Bastiaens, P., Caudron, M., Niethammer, P., and Karsenti, E. (2006). Gradients in the self-organization of the mitotic spindle. Trends Cell Biol. *16*, 125–134.

Bieling, P., Telley, I.A., Hentrich, C., Piehler, J., and Surrey, T. (2010). Fluorescence microscopy assays on chemically functionalized surfaces for quantitative imaging of microtubule, motor, and +TIP dynamics. Methods Cell Biol. *95*, 555–580.

Bornens, M., and Moudjou, M. (1999). Studying the composition and function of centrosomes in vertebrates. Methods Cell Biol. *61*, 13–34.

Cassimeris, L., Leung, J.C., and Odde, D.J. (2018). Monte Carlo simulations of microtubule arrays: The critical roles of rescue transitions, the cell boundary, and tubulin concentration in shaping microtubule distributions. PLOS ONE *13*, e0197538.

Castoldi, M., and Popov, A.V. (2003). Purification of brain tubulin through two cycles of polymerization-depolymerization in a high-molarity buffer. Protein Expr. Purif. *32*, 83–88.

Curmi, P.A., Maucuer, A., Asselin, S., Lecourtois, M., Chaffotte, A., Schmitter, J.M., and Sobel, A. (1994). Molecular characterization of human stathmin expressed in Escherichia coli: site-directed mutagenesis of two phosphorylatable serines (Ser-25 and Ser-63). Biochem. J. *300 (Pt 2)*, 331–338.

Curmi, P.A., Andersen, S.S., Lachkar, S., Gavet, O., Karsenti, E., Knossow, M., and Sobel, A. (1997). The stathmin/tubulin interaction in vitro. J. Biol. Chem. *272*, 25029–25036.

Deneubourg, J.-L. (1977). Application de l'ordre par fluctuations à la description de certaines étapes de la construction du nid chez les termites. Insectes Sociaux *24*, 117–130.

Dogterom, M., and Leibler, S. (1993). Physical aspects of the growth and regulation of microtubule structures. Phys. Rev. Lett. *70*, 1347–1350.

Gadea, B.B., and Ruderman, J.V. (2006). Aurora B is required for mitotic chromatin-induced phosphorylation of Op18/Stathmin. Proc. Natl. Acad. Sci. U. S. A. *103*, 4493–4498.

Gavriljuk, K., Itzen, A., Goody, R.S., Gerwert, K., and Kötting, C. (2013). Membrane extraction of Rab proteins by GDP dissociation inhibitor characterized using attenuated total reflection infrared spectroscopy. Proc. Natl. Acad. Sci. U. S. A. *110*, 13380–13385.

Grassé, P.-P. (1959). La Reconstruction du nid et les coordinations interindividuelles chez Bellicositermes natalensis et Cubitermes Sp. ; la théorie de la stigmergie : essai d'interprétation, comportement des termites constructeurs. Insectes Sociaux *6*, 41–81.

Grecco, H.E., Roda-Navarro, P., and Verveer, P.J. (2009). Global analysis of time correlated single photon counting FRET-FLIM data. Opt. Express *17*, 6493–6508.

Grecco, H.E., Roda-Navarro, P., Girod, A., Hou, J., Frahm, T., Truxius, D.C., Pepperkok, R., Squire, A., and Bastiaens, P.I.H. (2010). In situ analysis of tyrosine phosphorylation networks by FLIM on cell arrays. Nat. Methods *7*, 467–472.

Grieneisen, V. (2009). "Dynamics of auxin patterning in plant morphogenesis", thesis (University of Utrecht).

Guntas, G., Hallett, R.A., Zimmerman, S.P., Williams, T., Yumerefendi, H., Bear, J.E., and Kuhlman, B. (2015). Engineering an improved light-induced dimer (iLID) for controlling the localization and activity of signaling proteins. Proc. Natl. Acad. Sci. U. S. A. *112*, 112–117.

Hughes, L.D., Rawle, R.J., and Boxer, S.G. (2014). Choose Your Label Wisely: Water-Soluble Fluorophores Often Interact with Lipid Bilayers. PLoS ONE *9*, e87649.

Hyman, A., Drechsel, D., Kellogg, D., Salser, S., Sawin, K., Steffen, P., Wordeman, L., and Mitchison, T. (1991). Preparation of modified tubulins. Methods Enzymol. *196*, 478–485.

Jourdain, L., Curmi, P., Sobel, A., Pantaloni, D., and Carlier, M.F. (1997). Stathmin: a tubulin-sequestering protein which forms a ternary T2S complex with two tubulin molecules. Biochemistry *36*, 10817–10821.

Juniper, M.P.N., Weiss, M., Platzman, I., Spatz, J.P., and Surrey, T. (2018). Spherical network contraction forms microtubule asters in confinement. Soft Matter *14*, 901–909.

Koseska, A., and Bastiaens, P.I. (2017). Cell signaling as a cognitive process. EMBO J. *36*, 568–582.

Laan, L., Roth, S., and Dogterom, M. (2012). End-on microtubule-dynein interactions and pulling-based positioning of microtubule organizing centers. Cell Cycle Georget. Tex *11*, 3750–3757.

Litschel, T., Ramm, B., Maas, R., Heymann, M., and Schwille, P. (2018). Beating vesicles: Encapsulated protein oscillations cause dynamic membrane deformations. Angew. Chem. Int. Ed Engl.

Marée, A.F.M., Jilkine, A., Dawes, A., Grieneisen, V.A., and Edelstein-Keshet, L. (2006). Polarization and movement of keratocytes: a multiscale modelling approach. Bull. Math. Biol. *68*, 1169–1211.

Maturana, H.R., and Varela, F.J. (1980). Autopoiesis and cognition (Reidel).

Mitchison, T., and Kirschner, M. (1984). Dynamic instability of microtubule growth. Nature *312*, 237–242.

Munoz, A., Blu, T., and Unser, M. (2001). Least-squares image resizing using finite differences. IEEE Trans. Image Process. *10*, 1365–1378.

van Nies, P., Westerlaken, I., Blanken, D., Salas, M., Mencía, M., and Danelon, C. (2018). Self-replication of DNA by its encoded proteins in liposome-based synthetic cells. Nat. Commun. *9*, 1583.

Niethammer, P., Bastiaens, P., and Karsenti, E. (2004). Stathmin-tubulin interaction gradients in motile and mitotic cells. Science *303*, 1862–1866.

Niethammer, P., Kronja, I., Kandels-Lewis, S., Rybina, S., Bastiaens, P., and Karsenti, E. (2007). Discrete states of a protein interaction network govern interphase and mitotic microtubule dynamics. PLoS Biol. *5*, e29.

Noujaim, M., Bechstedt, S., Wieczorek, M., and Brouhard, G.J. (2014). Microtubules accelerate the kinase activity of Aurora-B by a reduction in dimensionality. PloS One *9*, e86786.

Pinot, M., Chesnel, F., Kubiak, J.Z., Arnal, I., Nedelec, F.J., and Gueroui, Z. (2009). Effects of confinement on the self-organization of microtubules and motors. Curr. Biol. CB *19*, 954–960.

Popp, M.W., Antos, J.M., Grotenbreg, G.M., Spooner, E., and Ploegh, H.L. (2007). Sortagging: a versatile method for protein labeling. Nat. Chem. Biol. *3*, 707–708.

Prigogine, I., and Nicolis, G. (1967). On Symmetry- Breaking Instabilities in Dissipative Systems. J. Chem. Phys. *46*, 3542–3550.

Rangamani, P., Lipshtat, A., Azeloglu, E.U., Calizo, R.C., Hu, M., Ghassemi, S., Hone, J., Scarlata, S., Neves, S.R., and Iyengar, R. (2013). Decoding information in cell shape. Cell *154*, 1356–1369.

Raspopovic, J., Marcon, L., Russo, L., and Sharpe, J. (2014). Modeling digits. Digit patterning is controlled by a Bmp-Sox9-Wnt Turing network modulated by morphogen gradients. Science *345*, 566–570.

Schmick, M., and Bastiaens, P.I.H. (2014). The interdependence of membrane shape and cellular signal processing. Cell *156*, 1132–1138.

Schmick, M., Vartak, N., Papke, B., Kovacevic, M., Truxius, D.C., Rossmannek, L., and Bastiaens, P.I.H. (2014). KRas localizes to the plasma membrane by spatial cycles of solubilization, trapping and vesicular transport. Cell *157*, 459–471.

Schrödinger, E. (1944). What is life? (UK: Cambridge University Press).

Sendra, G.H., Hoerth, C.H., Wunder, C., and Lorenz, H. (2015). 2D map projections for visualization and quantitative analysis of 3D fluorescence micrographs. Sci. Rep. *5*.

Sessa, F., Mapelli, M., Ciferri, C., Tarricone, C., Areces, L.B., Schneider, T.R., Stukenberg, P.T., and Musacchio, A. (2005). Mechanism of Aurora B activation by INCENP and inhibition by hesperadin. Mol. Cell *18*, 379–391.

Steinberg-Yfrach, G., Rigaud, J.L., Durantini, E.N., Moore, A.L., Gust, D., and Moore, T.A. (1998). Light-driven production of ATP catalysed by F0F1-ATP synthase in an artificial photosynthetic membrane. Nature *392*, 479–482.

Susnea, I., and Axenie, C. (2015). Cognitive Maps for Indirect Coordination of Intelligent Agents. Stud. Inform. Control *24*.

Tabony, J. (2006). Microtubules viewed as molecular ant colonies. Biol. Cell *98*, 603–617.

Theraulaz, G., Gautrais, J., Camazine, S., and Deneubourg, J.-L. (2003). The formation of spatial patterns in social insects: from simple behaviours to complex structures. Philos. Transact. A Math. Phys. Eng. Sci. *361*, 1263–1282.

Thévenaz, P., Ruttimann, U.E., and Unser, M. (1998). A pyramid approach to subpixel registration based on intensity. IEEE Trans. Image Process. Publ. IEEE Signal Process. Soc. *7*, 27–41.

Thom, R. (1994). Structural Stability And Morphogenesis (Westview Press).

Thomas, F.A., Visco, I., Petrášek, Z., Heinemann, F., and Schwille, P. (2015). Introducing a fluorescence-based standard to quantify protein partitioning into membranes. Biochim. Biophys. Acta *1848*, 2932–2941.

Zaytsev, A.V., Segura-Peña, D., Godzi, M., Calderon, A., Ballister, E.R., Stamatov, R., Mayo, A.M., Peterson, L., Black, B.E., Ataullakhanov, F.I., et al. (2016). Bistability of a coupled Aurora B kinase-phosphatase system in cell division. ELife *5*, e10644.

METHODS

Preparation of recombinant proteins

Amino acid sequences of all used constructs are presented in Table S2. All proteins were expressed in *E. coli* BL21 DE3 RIL over night at 18 °C after induction with 0.2 mM IPTG. AuroraB was bicistronically expressed with the INCENP in-box from a modified pGEX6P-2rbs plasmid, which was a gift from A. Musacchio. All other proteins were expressed from a pET24 plasmid as fusions to an N-terminal His_{10}-tag followed by a TEV protease site. 4 – 6 liters of LB medium were used to express Stathmin, iLID, and λ-phosphatase (λ-PPase), whereas 10 – 12 liters of TB medium were used for AuroraB. Cells were lysed by two passes through an Emulsiflex C5 (Avestin, Mannheim, Germany), and the lysate was cleared by 45 – 60 min centrifugation at 20000 rpm in an A27-8x50 rotor (Sorvall/Thermo Fisher Scientific, Dreieich, Germany).

Stathmin and iLID

Gly-Stathmin-Cys, Gly-iLID-tRac1, or Gly-C2-iLID were purified via Ni-NTA Superflow (Qiagen, Hilden, Germany) in 50 mM NaP_i pH 8, 300 mM NaCl, 2 mM $MgCl_2$, 0.1 mM β-mercaptoethanol, 10 mM imidazole. The column was washed with 60 mM imidazole, and the protein eluted by a step to 500 mM imidazole. The eluate was supplemented with 2 – 4 mg TEV protease and dialyzed over night against 2 L of 50 mM Tris pH 8, 100 mM NaCl, 1 mM EDTA, 0.1 mM β-mercaptoethanol. The cleaved protein was adjusted to 10 mM imidazole (60 mM for Gly-C2-iLID), and passed again through the Ni-NTA column, followed by gel filtration on a HiLoad 26/600 Superdex 75 pg column (GE Healthcare, Solingen, Germany) in 50 mM Hepes pH 7.5, 200 mM NaCl, 2 mM $MgCl_2$, 2 mM DTT. For iLID constructs, the sample was adjusted to a saturated concentration of flavin mononucleotide prior to gel filtration. Gly-iLID-tRac1 was subsequently geranylgeranylated as described elsewhere (Gavriljuk et al., 2013). We refer to geranylgeranylated iLID as iLID_G.

λ-phosphatase

The protein was purified via cobalt-loaded HiTrap Chelating HP columns (GE Healthcare) in 50 mM NaP_i pH 8, 500 mM NaCl, 2 mM $MgCl_2$, 5 % v/v glycerol, 0.1 mM β-mercaptoethanol, 10 mM imidazole. The washing/elution steps were 60, 200, 500 mM imidazole. The eluted protein was quickly supplemented with 10 mM DTT and digested with TEV protease as above, while dialyzing against 2 L of 50 mM Tris pH 8, 500 mM NaCl, 5 % v/v glycerol, 2 mM $MgCl_2$, 10 mM DTT. The cleaved protein was buffer exchanged back into the sodium phosphate buffer via a HiPrep Desalting 26/10 column (GE Healthcare), adjusted to 10 mM imidazole, and passed again over the chelating column. Finally, the protein was gel filtered on a HiLoad 26/600 Superdex 75 pg column (GE Healthcare) in 50 mM Hepes pH 7.5, 500 mM NaCl, 2 mM $MgCl_2$, 5 mM DTT, 10 % v/v glycerol.

AuroraB

Gly-SspB-AuroraB(45-344)/INCENP(834-902) was purified via Glutathione Sepharose 4 Fast Flow (GE Healthcare) in 50 mM Hepes pH 7.3, 500 mM NaCl, 2 mM $MgCl_2$, 5 mM DTT, 5 % v/v glycerol. The column with bound protein was washed with buffer containing 1 mM ATP, then the protein was eluted with buffer containing 20 mM glutathione and additional DTT up to 10 mM. The protein was cleaved over night with TEV protease while remaining in the elution buffer. The cleaved protein was buffer exchanged via a HiPrep Desalting 26/10 column (GE Healthcare) to remove glutathione, and passed again through the Glutathione Sepharose column. Gel filtration was carried out on a HiLoad 26/600 Superdex 200 pg column (GE Healthcare) in

50 mM Hepes pH 7.3, 500 mM NaCl, 2 mM $MgCl_2$, 5 mM DTT avoiding concentrating the protein before gel filtration. Finally, the protein was concentrated in an Amicon Stirred Cell (Merck Millipore, Darmstadt, Germany), adjusted to 20% glycerol and hard spun at 400.000 g prior to shock freezing.

Preparation of tubulin and centrosomes

Tubulin purification was performed according to a standard method (Castoldi and Popov, 2003). The following deviations from the published procedure were made: the ratio of buffer/brain mass was 1.5 l/kg, and the Pipes final concentration in the polymerization steps was 333 mM. Purified tubulin was adjusted to a concentration of 200 µM with BRB80 (80 mM Pipes pH 6.8, 1 mM $MgCl_2$, 1 mM EGTA) and stored at –150 °C.

Tubulin was labeled with NHS-Alexa568 or -647 (Thermo Fisher Scientific) or EZ-link NHS-biotin (Thermo Fisher Scientific) according to a standard procedure(Hyman et al., 1991). Typically, 50 mg of tubulin were labeled with a 7.5-fold molar excess of dye assuming 70 % tubulin recovery after the initial polymerization step. Following deviations from the published procedure were made: the dye was added in two steps, each followed by a 15 min incubation, totaling 40 µl DMSO in 1 ml buffer. The reaction was not specifically stopped, and all ultracentrifugation steps were performed at an increased speed of 400.000 g in an MLA-80 rotor (Beckman Coulter, Krefeld, Germany). Labeled tubulin was adjusted to 200 µM with BRB80 and stored at –150 °C.

Centrosomes were isolated from KE37 cells following a standard method (Bornens and Moudjou, 1999).

Protein labeling

Proteins were specifically labeled by sortagging (Popp et al., 2007). The LPETGG peptide was conjugated to NHS-Alexa488, -647, or Atto532 over night at 30 °C (20 mM peptide, 40 mM dye (Thermo Fisher Scientific for Alexa dyes, Atto-tec (Siegen, Germany) for Atto532) in DMSO), the reaction stopped by 100 mM Tris pH 8. Typically, 1 – 3 mg protein (ideally around 300 µM final concentration in the reaction), were mixed with a 4-fold excess of conjugated peptide, ca. 100 µM Sortase A (from *S. aureus*, gift from P. Bieling), and 6 mM $CaCl_2$. For iLID constructs, the sample was additionally adjusted to a saturated concentration of flavin mononucleotide. The reaction was allowed to proceed over night at 18 °C or 4 °C (for λ-PPase and AuroraB), and the mixture was separated by gel filtration on a Superdex 75 10/300 GL column (GE Healthcare) in appropriate protein gel filtration buffer.

Protein encapsulation in GUVs by cDICE

Encapsulation of proteins in GUVs was achieved by continuous Droplet Interface Crossing Encapsulation following the original method (Abkarian et al., 2011) with relevant parameters noted below. Empty GUVs used for experiments in the outside configuration were also produced by this method.

0.36 mM lipids were prepared in mineral oil (M3516, Sigma Aldrich/Merck, Darmstadt, Germany). The mixture consisted of eggPC (Sigma Aldrich/Merck) with 15 mol% DOPS and 0.05 mol% DOPE-biotin (both from Avanti Polar Lipids, Alabaster, U.S.A.). Glass capillaries were typically 10 – 15 µm wide, and pressure was applied using an MFCS-EZ control system (Fluigent, Jena, Germany). cDICE chambers were 3.5 cm wide and were rotated at 1500 – 1800

rpm. 8-well Lab-Tek chambers (Thermo Fisher Scientific) or 18-well μ-slides (ibidi, Martinsried, Germany) were coated with streptavidin for GUV immobilization.

The base cDICE buffer contained 80 mM Pipes pH 6.8, 75 mM KCl, 2 mM $MgCl_2$, 1 mM EGTA, 1 mM trolox, 0.1 mg/ml β-casein. Additionally, the inner buffer contained 300 mM sucrose and 80 mM glucose, while the outer buffer contained 380 mM glucose. Whenever an osmotic deflation of GUVs to decrease membrane tension was desired, the sucrose concentration inside was lowered by 50 mM and the outside glucose concentration was increased by the same amount (i.e. Figure 1A center, Figures 4, 5, 6).

In experiments involving λ-PPase, EGTA was replaced by 0.8 mM $MnCl_2$. For tubulin polymerization, 2 mM GTP was included, whereas phosphorylation gradient experiments just required the presence of soluble tubulin, for which 60 μM GTP were included. For AuroraB, 2 mM ATP was added, and in experiments requiring both nucleotides the $MgCl_2$ concentration was increased to 4 mM. Oxygen scavengers (see "Single-filament TIRF microscopy and data analysis") were included in cases with just microtubule asters and stathmin, but were omitted in all other encapsulation experiments.

The encapsulation efficiency of tubulin and stathmin was determined by a reference concentration outside of GUVs (Figure S2D), and the used protein concentration in cDICE was adjusted to yield desired final concentrations, as indicated in respective experiments. For encapsulation of centrosomes, the samples typically contained 10 vol% of a purified centrosome fraction.

For the encapsulation of iLID, AuroraB, and λ-PPase, an exact concentration was not targeted, but the resulting inside concentrations and membrane densities given specific starting concentrations were quantified (Figure S3D) and verified to result in sufficient membrane recruitment and desired stathmin phosphorylation state (see "Imaging and quantification of light-induced protein translocation" and "Measurement and analysis of local stathmin phosphorylation gradients").

Prior to cDICE, the samples were centrifuged for 15 min at 100.000 rpm in a TLA-100 rotor (Beckman Coulter). The centrosomes were never centrifuged, while the tubulin stock was centrifuged separately for 30 min at 60.000 rpm in an RP80-AT2 rotor (Sorvall/Thermo Fisher Scientific).

Imaging of MT asters and morphological states in GUVs

To produce MT asters in GUVs, soluble tubulin and centrosomes were encapsulated as described in "Protein encapsulation in GUVs by cDICE". Stathmin was included as indicated for individual experiments. The following protein concentrations were used in the full reconstituted morphogenic system: 40 or 44 μM (final) tubulin (10 % Alexa647-tubulin), 4 μM (final) stathmin, 5 μM Gly-C2-iLID, 12 μM Alexa488-SspB-AuroraB/INCENP, 1 μM λ-PPase. Alexa568-tubulin was used for all other experiments at indicated concentrations.

Imaging was done on a Leica SP8 confocal microscope (Leica Microsystems, Wetzlar, Germany) equipped with Leica HyD hybrid detectors at 33 °C in an environment-controlled chamber (Life Imaging Services, Basel, Switzerland) using an HC PL APO 63x/1.2NA motCORR CS2 water objective (Leica Microsystems). The elevated temperature promoted tubulin polymerization, the asters reaching their end state in ca. 7 minutes, after which single-plane images or z-stacks (1 or 0.5 μm spacing) were taken. For the temperature ramp experiments, GUV-containing Lab-Tek chambers were incubated at 4 °C for 10 minutes in the pre-cooled Stable Z Lab-Tek Stage (Bioptechs, Butler, U.S.A.). Then, the stage was moved onto

the microscope equilibrated at room temperature and reached RT (~ 21 °C) in 10 minutes. The measurements indicated as "cold" were done under this condition. After that the Stable Z Lab-Tek Stage controller was used to heat the sample to 34 °C within 20 minutes and images were taken every minute.

Alexa568 was excited with a 470 – 670 nm white light laser (white light laser Kit WLL2, NKT Photonics, Köln, Germany) at 578 nm. Detection of fluorescence emission was done in standard mode, restricted with an Acousto-Optical Beam Splitter (AOBS) to 588 – 640 nm. Images were taken with 4x line averaging at 400 or 200 Hz scanning speed. The pinhole was set to 1 Airy unit here and in all experiments described in this work.

In the full morphogenic system, Alexa647 was excited at 650 nm at 1000 Hz scanning speed to reduce photodamage. Detection of fluorescence emission was done in counting mode, restricted to 650 – 750 nm and further restricted by LightGate time-gating to minimize signal from laser reflection and background. Activation of iLID and imaging of Alexa488-SspB-AuroraB was done with 488 nm excitation from a white light laser source, restricting detection to 498 – 580 nm and by LightGate. Time series images and stacks (1 µm spacing) were taken with 8x line accumulation in line sequential scanning mode. For local activation, 488 nm illumination was restricted to a manually drawn ROI.

Single-filament TIRF-M assay and data analysis

GMPCPP-stabilized microtubule seeds were prepared asfollows: 40 µL of 40 µM tubulin mixture (25 % tubulin, 25 % Alexa568-tubulin, 50 % biotinylated tubulin) was polymerized in seed buffer (80 mM Pipes pH 6.8, 1 mM $MgCl_2$, 1 mM EGTA, 1 mM GMPCPP (Jena Bioscience), 5 mM β-mercaptoethanol) at 37 °C. After 30 minutes, 400 µL of prewarmed BRB80 (80 mM Pipes pH 6.8, 1 mM $MgCl_2$, 1 mM EGTA) was added to the tubulin mixture, which was then spun down in a table top centrifuge at 21.000 g for 8 minutes at RT. The microtubule pellet was thoroughly resuspended in 40 µL of BRB80.

TIRF flow chambers were assembled from a biotin-PEG functionalized glass coverslip attached to a PLL-PEG passivated cover slide using double-sided tape (Bieling et al., 2010). To prevent potential unspecific binding, the flow chamber was first flushed and incubated with 35 µL of blocking buffer (100 β-casein µg/mL, 1 % w/v Pluronic F-127 in assay buffer (40 mM Pipes pH 6.8, 75 mM KCl, 4 mM $MgCl_2$, 0.4 mM EGTA, 1 mM GTP, 100 β-casein µg/mL, 1 mM trolox, 20 mM β-mercaptoethanol). After 5 minutes, the flow chamber was washed two times with 35 µL of assay buffer. Then, the chamber was flushed and incubated with 35 µL of 150 µg/mL Neutravidin (Thermo Fisher Scientific) in assay buffer for another 5 minutes. The flow chamber was washed two times with 35 µL of assay buffer, and then the chamber was flushed and incubated with 35 µL of diluted (1:750) GMPCPP-stabilized microtubule seeds. After 5 minutes, the chamber was washed two times with 35 µL of assay buffer.

After the seeds were immobilized on the surface, 40 µL of protein mixture (10 – 40 µM tubulin (7.5 % Alexa568-labeled), 0 – 20 µM stathmin, 0 – 30 µM phospho-stathmin, 4 µL 10x oxygen-scavenging system (Bieling et al., 2010), 0. 2% w/v methylcellulose) in assay buffer was introduced into the flow chamber and the two sides were sealed with transparent nail polish.

Imaging was performed at RT with a custom-built TIRF microscope (Olympus IX81 base) with a 60x Olympus APON TIRF objective with TOPTICA IBeam smart 560s laser and a Quad-Notch filter (400-410/488/561/631-640). Temperature was kept at 34 °C by a collar objective heater (Bioptechs). Image acquisition was done with an EM CCD Andor iXon 888 camera controlled by Micromanager 1.4 software. Fiji ImageJ was used for data analysis. For each

condition, the average growth velocity and catastrophe frequency were determined from ≥60 microtubules by kymograph analysis.

Determination of MT-aster size *in vitro*

20 µL of protein mixture (10 – 40 µM tubulin (7.5% Alexa568-labeled), 0 – 20 mM stathmin, 0 – 30 µM phospho-stathmin, 2 µl Silica beads (SS06N, Bangs Laboratories, Fishers, U.S.A.), 2 µl 10x oxygen-scavenging system(Bieling et al., 2010), 0.2 % w/v methylcellulose) was dispersed on a glass cover slide blocked with PLL-PEG(Bieling et al., 2010) and covered with a glass coverslip pre-coated with PLL-PEG. The edges were sealed with transparent nail polish. Imaging of asters at 33 °C or in temperature ramp experiments were done as described in "Imaging of microtubule asters and morphogenic state transitions in GUVs". 12 µm thick z-stacks (1 µm spacing) were taken in the experiments at 33 °C, but single planes were taken during the temperature ramp to maximize the number of imaged fields of view.

For each individual condition, the z-stacks (if present) of each position were average projected in Z and aligned on each other, and projected again using a custom macro in ImageJ. The radial intensity profile of the averaged data (> 30 asters per condition) was extracted with a custom ImageJ macro. The aster size was determined as the 99 % decay length of a mono-exponential fit to the radial intensity profile in Origin (OriginLab, Northhampton, U.S.A.).

Morphometric analysis of GUVs

Centrosome Position and Eccentricity

A mask of the GUVs was obtained by thresholding the fluorescence intensity of fluorescently labeled tubulin at the plane of the centrosome and an ellipse was fitted to the mask in ImageJ. The centrosome position relative to the center of mask was calculated by:

$$Relative\ Centrosome\ Position = \frac{\left|\bar{r}_c - \bar{r}_{guv}\right|}{R_{guv}}$$

where $\bar{r}_c = (x_c, y_c)$ and $\bar{r}_{guv} = \left(x_{guv}, y_{guv}\right)$ are the position of the centrosome and the geometric center of the fitted ellipse obtained in ImageJ, respectively, and $R_{guv} = (M + m)/4$ where M and m are the major and minor axis of the ellipse. The eccentricity of the fitted ellipse was calculated as:

$$e = \sqrt{1 - \frac{m^2}{M^2}}.$$

Modified roundness was calculated as:

$$R^* = \frac{1}{Ro * \frac{M}{F}}$$

where Ro and F are the roundness and the Feret diameter of the mask, respectively, obtained in ImageJ.

Morphometric kymographs

At each time point of the SynMPS time lapse experiments, a mask of the SynMPS shape was made in the fluorescently labeled tubulin image, by performing a 2-pixel Gaussian Blur and thresholding. Masks and CLSM images were imported in MATLAB 2017b. At each time point, a circle was fitted to the mask edge. The angles of each edge pixel were calculated with respect to the geometric center of the fitted circle by trigonometry, while their distance to the fitted circle was calculated by

$$d(\theta, t) = |\bar{r}(\theta, t) - \bar{r}_c(t)| - R(t)$$

where $\bar{r}(\theta, t)$ are the positions of the pixel in the edge of the mask, and $\bar{r}_c(t)$ and $R(t)$ are the center and radius of the fitted circle at time t. The matrix $d(\theta, t)$ was then exported to TIFF and overlaid with the fluorescence intensity kymographs in ImageJ.

For the Alexa488-SspB-AuroraB fluorescence intensity kymographs, a similar procedure as for the morphometric kymographs was employed. In this case, the masks were eroded and dilated using imerode and imdilate respectively, to smooth out protrusions and forming a band following the shape of the SynMPS excluding the protrusions.

Imaging and analysis of light-induced translocation

Imaging of light-induced translocation of SspB-AuroraB (Alexa488- or Alexa647-labeled) or Alexa647-SspB-λ-PPase to membrane-bound iLID (Alexa488-labeled or unlabeled) was done on a Leica SP8 confocal microscope (see "Imaging of microtubule asters and morphogenic state transitions in GUVs"). iLID was activated by the 458 nm Argon laser line. Alexa647 and Alexa488 were excited with 650 and 495 nm white line laser lines, respectively. Detection of fluorescence emission was done in photon counting mode, restricted with an Acousto-Optical Beam Splitter (AOBS) (505 – 560 nm for Alexa488, 660 – 700 nm for Alexa647), and further restricted by LightGate time-gating to minimize signal from laser reflection and background. Images were taken in sequential frame mode when using Alexa647-labeled proteins, where the 488 nm channel would be used to activate iLID and also image it in the cases when iLID was also labeled. For the translocation of Alexa488-labeled SspB-AuroraB, unlabeled iLID was used, and only images of the 488 nm channel were taken to simultaneously activate iLID and image SspB-AuroraB. Typically for activation, it was sufficient to take an image in the 488 nm channel every 3 – 4 s, but sometimes higher framerates (ca. 0.6 s) were used to fully resolve the kinetics in time and also to maximize the light dose. Since, iLID inactivation kinetics occur on minute timescale, it was sufficient to sample these every 3 – 4 s.

For the outside experiments, varying protein concentrations were added to immobilized GUVs as indicated in individual figure legends. We mainly used C2-iLID, but we found no general differences in the behavior of the prenylated iLID_G in respect to recruitment and unbinding kinetics as well as to achievable surface densities of the effector proteins. The defined protein concentration in the bulk was used to calculate the protein densities on the membrane using a semi-automated tool in Matlab (MathWorks, Natick, U.S.A.) (Thomas et al., 2015). Bulk depletion effects could be neglected because only 10 – 50 GUVs were present in each 50 µl sample. Binding and unbinding kinetics were exponentially fit in Origin (OriginLab).

For inside GUV experiments, defined starting concentrations are indicated in individual figure legends. To quantify the encapsulation efficiency and membrane densities, a defined

protein concentration was added outside of the GUVs as a reference. Analysis was done in the same manner as for outside GUV experiments.

Analysis of AuroraB clustering

The CFLSM time lapse images were imported into Fiji. Time lapse images were registered using the Plugin "MultiStackReg v1.45". A circular ROI was drawn at the GUV membrane. The circular ROI was converted into a series of segments, the line width set to 20 pixels to form a band at the GUV membrane. The circular band was straightened for each image in the time lapse and the intensity profiles of the straightened time lapse were imported to MATLAB 2017b and plotted with pcolor.

For the analysis of the regularity of Alexa488-SspB-AuroraB clusters we linearized the equatorial planes of GUV images with an 8 – 12 pixels wide mask around the membrane. To analyze the two activation series in a comparable manner, we used every sixth image of the high light dose series (thus averaging 10 out of 60 frames), and ten images within the low light dose series (frames 25 – 34 of 46, thus not picking the frames immediately after the end of the high light dose series). In this manner, the frame interval was 4 s for both doses and the same number of frames were used to keep the signal-to-noise ratio consistent. The images were then resized to a total length of 1024 pixels with the Resize plugin (Munoz et al., 2001) for ImageJ. The power spectrum was then calculated by a Fast Fourier Transformation in ImageJ and the spectrum along the x-axis was further processed in Origin (OriginLab). One of the identical sides of the two-sided power spectrum was further used, and the first datapoints dominated by the 0-frequency component (DC-value) were discarded. The spectrum was then normalized to the sum of all values. Due to the sampling interval being one pixel and all images being normalized to 1024-pixel length, the frequency axis ranges from 0 – 0.5 $pixel^{-1}$ for all GUVs, allowing averaging. Distinct peaks indicate regularities in the spatial organization of SspB-AuroraB clusters. To convert the frequency to a more visual measure, the frequency can be multiplied by the total number of sampling points, namely 1024 pixels. This gives the number of regularly organized features/clusters in the observed plane.

To analyze the persistence of SspB-AuroraB clusters, the recovery, meaning the time dependent unbinding of SspB-AuroraB from iLID in the dark, was measured. A threshold intensity was determined to classify membrane-bound SspB-AuroraB in two species, called "clustered" (≥ 20 counts) and homogeneous (< 20 counts). The average intensity for each time point was calculated for both species and normalized to the first time-point.

$COPY^o$ characterization

Gly-Stathmin-Cys was sequentially labeled with two organic dyes to generate the sensor $COPY^o$ (^{o} = organic). First, the acceptor dye was conjugated to the C-terminal cysteine. Typically, 3 mg of Gly-Stathmin-Cys were incubated with 5 mM TCEP for 1 h at room temperature under an argon atmosphere before buffer exchange via a NAP5 column (GE Healthcare) into degassed 50 mM Hepes pH 7.5, 200 mM NaCl, 2 mM $MgCl_2$. A 10-fold molar excess of Atto655-maleimide (Atto-tec) was added and the mixture incubated for 3 h at room temperature under an argon atmosphere. The reaction was stopped by adding 5 mM DTT. Next, without further purification, the donor dye Atto532 (Atto-tec) was conjugated to the N-terminus as described in the section "Protein labeling". Another sensor version was constructed with Atto647N (Atto-tec) as acceptor dye, which we termed $COPY^{o2}$.

Initial characterization was carried out by evaluating sensitized emission (Figure S5A). Fluorescence emission spectra were measured with a QuantaMaster fluorescence system (PTI) (exc. 520 nm, em. 530 – 720 nm). 1 µM sensor was in 80 mM Pipes pH 6.8, 75 mM KCl, 1 mM EGTA, 2 mM $MgCl_2$, 20 mM β-mercaptoethanol. 10 µM tubulin was added to measure the decrease of sensitized emission.

Detailed characterization of the FRET properties was done by analysis of donor fluorescence lifetime. Confocal FLIM experiments were performed on a Leica SP8 confocal microscope (see "Imaging of microtubule asters and morphogenic state transitions in GUVs") equipped with the FALCON (FAst Lifetime CONtrast) system. Atto532 was excited at 532 nm with a pulse frequency of 40 MHz and emission was collected with three Leica HyD detectors restricted with an Acousto-Optical Beam Splitter (AOBS) to 542 – 563, 568 – 591, and 591 – 620 nm. Data were collected for the donor-only labeled Stathmin, free $COPY^{o}$ and $COPY^{o2}$ (3 µM), and tubulin-bound sensors (+ 20 µM tubulin) in cDICE base buffer (see "Protein encapsulation in GUVs by cDICE") + 60 µM GTP, 300 mM sucrose, and additional 1 mM trolox. Photons were collected up to approx. 3000 photons per pixel in the sum of all three detectors. Global analysis of FLIM-FRET was implemented in a custom program written in Python according to a described process (Grecco et al., 2009, 2010), yielding τ_D (ns) and τ_{DA} (ns) as well as FRET efficiency. Additionally, all pixel values of the output lifetime images were averaged to obtain the absolute lifetimes of the donor for the free and tubulin-bound sensor states (Figure S5B).

Due to the higher signal amplitude obtainable with $COPY^{o2}$, we preferred this variant for stopped-flow and most kinetic measurements. However, since Atto647N (acceptor dye in $COPY^{o2}$) is positively charged and is known to interact with membranes (Hughes et al., 2014), we used $COPY^{o}$ for the measurement of stathmin phosphorylation gradients.

Stopped-flow measurements

Association and dissociation of $COPY^{o2}$ and tubulin were measured in a stopped flow apparatus (Applied Photophysics, Leatherhead, U.K.) with excitation at 535 nm and a 670/30 nm band-pass filter to monitor sensitized emission changes at 25 °C in 80 mM Pipes pH 6.8, 75 mM KCl, 2 mM $MgCl_2$, 20 mM β-mercaptoethanol, 60 µM GTP. $COPY^{o2}$ or phosphorylated $COPY^{o2}$ (see "Time-resolved measurements of AuroraB and λ-PPase activity") was kept constant at 200 nM for the tubulin titration. Dissociation was measured at 200 nM $COPY^{o2}$ and 4 µM tubulin, displacing $COPY^{o2}$ with 60 µM unlabeled stathmin. Data were fit in Origin (OriginLab), and error propagation for derived constants was calculated by Gaussian equation taking the errors of the fit as a starting point.

Determination of enzymatic kinetic parameters

Stathmin phosphorylation and dephosphorylation kinetics were measured using the fluorescence lifetime change of $COPY^{o}$ or $COPY^{o2}$ as indicated in the respective figure legends. Confocal FLIM measurements were performed as described for "Stathmin FRET sensor generation and characterization" with few modifications. Excitation pulse frequency was 20 MHz. Per time-point 1 – 2 million photons were collected in a 256x256 pixels image. During analysis, 4x binning was applied. Measurements were conducted in cDICE-buffer (see "Protein encapsulation in GUVs by cDICE") + 60 µM GTP, 300 mM sucrose, – EGTA, and + 0.8 mM $MnCl_2$ when λ-PPase was used.

To measure dephosphorylation kinetics, COPY^o was pre-phosphorylated (COPY^o-P) with 500 nM AuroraB by incubating with 4 mM ATP for 8 h at room temperature and used without further purification. Residual kinase activity was neglected because AuroraB partially loses its activity during the incubation, and also because λ-PPase deactivates AuroraB in the final sample for the kinetic measurement. Kinetic traces of dephosphorylation were obtained at varying concentrations of COPY^o-P (with tubulin present in at least two-fold excess) and 200 nM λ-PPase. Values for k_{cat} and K_m were determined from a fit to the Michaelis-Menten equation. Reported errors are errors of the fit, and the error for k_{cat}/K_m was derived by Gaussian error propagation.

Since phosphorylation of stathmin under conditions suitable for Michaelis-Menten analysis was too slow to yield sufficiently stable and analyzable signal amplitudes, we estimated k_{cat}/K_m from monoexponential fits of single-progress curves. 10 µM COPY^{o2} (+ 20 µM tubulin) was phosphorylated by 500 nM or 1 µM SspB-AuroraB, and the data were fit mono-exponentially. The apparent rate constant was converted to a value corresponding to k_{cat}/K_m by taking the used kinase concentrations into account and averaging the two obtained values. Fit errors were propagated by the Gaussian equation.

Note that the derived kinetic parameters for λ-PPase and SspB-AuroraB do not consider the presence of multiple phosphorylation sites on stathmin or how many of them need to be phosphorylated to induce tubulin dissociation. The parameters apply for the catalysis of the overall transition between free and tubulin-bound stathmin, which is our direct readout and also the relevant state change for the derivation of the signaling gradient.

Measurement of stathmin phosphorylation gradients

Spatial COPY^o phosphorylation gradients were imaged and quantified by computing the ratio of Atto655/Atto532 fluorescence emission intensities. First, we derive the relationship between the fluorescence FRET ratio to the fraction of tubulin bound stathmin.

The fluorescence intensity detected at the acceptor channel F_A can be separated into three contributions:

$$F_A = k_A[S] + K_{FA}^{pS}[pS] + K_{FA}^{tS}[tS]$$

where: k_A is a constant proportional to the fluorophore brightness, $[S]$ is the total stathmin concentration, and its product represents the intensity in absence of donor; K_{FA}^{pS} and K_{FA}^{tS} are the contributions to the intensity due to FRET when stathmin is either phosphorylated or tubulin bound, while $[pS]$ and $[tS]$ are their concentrations, respectively. We assume that stathmin can only adopt these two states and hence $[S] = [pS] + [tS]$.

The fluorescence at the donor channel F_D can be written as:

$$F_D = \frac{k_D[S]}{k_D[S] + K_{FD}^{pS}[pS] + K_{FD}^{tS}[tS]}$$

where k_D is a constant proportional to the donor fluorophore brightness, and K_{FD}^{pS} , K_{FD}^{tS} are the contributions to donor quenching by FRET, in the corresponding stathmin states.

Normalizing the acceptor fluorescence intensity to the total stathmin concentration yields:

$$\frac{F_A}{[S]} = k_A + K_{FA}^{pS}(1-\alpha) + K_{FA}^{tS}\alpha$$

where $\alpha = [tS]/[S]$ is the fraction of tubulin bound stathmin. After rearranging terms, we obtain:

$$\frac{F_A}{[S]} = \left(k_A + K_{FA}^{pS}\right) + \alpha(K_{FA}^{tS} - K_{FA}^{pS})$$

Taking the FRET fluorescence ratio of acceptor fluorescence to donor fluorescence can be then expressed as:

$$cR = \frac{k_D}{[S]}\frac{F_A}{F_D} = \left[\left(k_A + K_{FA}^{pS}\right) + \alpha(K_{FA}^{tS} - K_{FA}^{pS})\right]\left[\left(k_D + K_{FD}^{pS}\right) + \alpha(K_{FD}^{tS} - K_{FD}^{pS})\right]$$

where $R = F_A/F_D$ is the fluorescence FRET ratio and $c = k_D/[S]^2$ is a constant. Grouping the remaining constants between parenthesis as,

$$\begin{aligned} K_A &= k_A + K_{FA}^{pS} \\ K_{FA} &= K_{FA}^{tS} - K_{FA}^{pS} \\ K_D &= k_D + K_{FD}^{pS} \\ K_{FD} &= K_{FD}^{tS} - K_{FD}^{pS} \end{aligned}$$

simplifies the expression to:

$$cR = [K_A + \alpha K_{FA}][K_D + \alpha F_{FD}]$$

Distributing the product yields:

$$cR = K_A K_D + \alpha(K_{FA}K_F + K_{FD}K_A) + \alpha^2 K_{FA}K_{FD}$$

Since the FRET efficiency of COPY^o is < 30 %, K_{FA}^{tS} is negligible, and the quadratic term becomes negligible, so we can solve for α as:

$$\alpha = \frac{cR - K_A K_D}{(K_{FA}K_F + K_{FD}K_A)}$$

Therefore, the fraction of tubulin bound stathmin α is an approximate linear function of the fluorescence FRET ratio R.

Confocal imaging was done on a Leica SP8 microscope (see "Imaging of microtubule asters and morphogenic state transitions in GUVs"). COPY^o was excited at 532 nm, and detection was done in photon counting mode, restricted to 542 – 560 nm and 640 – 750 nm for donor and acceptor, respectively. The imaging focus was maintained by Leica Adaptive Focus Control. Imaging conditions were identical when measuring outside of or inside GUVs. The following protein concentrations were used for encapsulation: 40 μM (final) tubulin, 4 μM (final) COPY^o, 5 μM C2-iLID, 12 μM SspB-AuroraB (unlabeled), 1 μM λ-PPase. Outside GUVs the following

concentrations were used: 20 µM tubulin, 10 µM COPY^{o}, 1 µM iLID_G, 1.5 µM SspB-AuroraB (unlabeled), and varying λ-PPase concentrations as indicated.

For the "dark" state (no iLID activation, no SspB-AuroraB translocation) 40 images at the equatorial plane were taken with 3 s intervals. This spacing was necessary to prevent unwanted iLID activation by 532 nm light. Inside GUVs, this illumination still led to substantial iLID activation, so that no gradient images for the dark state were obtained. Note that Figure 3F also only shows outside gradients in the activated state.

Activation of iLID was done with the 458 nm Argon laser line for the duration of 3 min with 3 s intervals. This sustained activation was performed to allow SspB-AuroraB to undergo full autoactivation and the steady-state of stathmin phosphorylation to be reached. iLID autofluorescence was detected between 568 – 520 nm to be used as a membrane marker during the analysis.

For the activated state, 40 images were taken with minimal intervals. A sequential line scan was performed between iLID activation and COPY^{o} imaging in order to maintain SspB-AuroraB translocation.

In case there was any GUV movement during dark or activated image series acquisition, the frames were aligned in ImageJ using the MultiStackReg plugin based on StackReg (Thévenaz et al., 1998). Then, all images of the series were summed up (more precise than averaging, and made possible by photon counting). We observed an optical xy-aberration between the donor and acceptor channels, which led to asymmetric edge effects around the GUVs in the ratio image. To avoid these, the channels were manually registered to yield a symmetric ratio image calculated as acceptor/donor. Radial profiles were extracted from the ratio images by a custom macro in ImageJ using iLID autofluorescence as a marker to determine the starting position at the membrane and align the profiles of individual GUVs.

Data obtained in this manner were sufficient to describe gradients arising outside of GUVs. Due to lower surface densities of recruited SspB-AuroraB inside GUVs, strong gradients only arose at the positions of SspB-AuroraB clusters. Radial averaging of a single confocal plane thus resulted in profiles with low gradient amplitudes. To visualize the gradient amplitude in cluster vicinity, we measured 7 – 8 µm thick z-stacks of the ratio (1 µm spacing, 10 images per slice) on sufficiently large GUVs at their equatorial plane, so that the GUV diameter would not significantly change throughout the stack. Maximum intensity projections along the z-axis were done to highlight gradient hotspots. 2D maps of the GUV surface were projected from the stacks using the Map3-2D software (Sendra et al., 2015).

Generic model for stigmergy

The stigmergic mechanism can be generically described with a two-component substrate-depletion model:

$$\frac{\partial u}{\partial t} = f(u,v) + D_u \frac{\partial^2 u}{\partial x^2}$$
$$\frac{\partial v}{\partial t} = -f(u,v) + D_v \frac{\partial^2 v}{\partial x^2} \qquad \text{(Eqs.1)}$$

where $u + v = c = const.$, u corresponds to the sand pillar structures (Figure 7A), the protein clusters on the membrane (Figure 7B) or the self-amplified MT-bundles that generate membrane deformations (Figure 7C), whereas v represents the respective free sand grains, protein monomers or astral MTs. To characterize the dynamical transitions in this system, we applied Linear Perturbation Analysis (LPA) (Grieneisen, 2009; Marée et al., 2006) that in turn allows to analyze the bifurcation structure of a reaction-diffusion (RD) system. In brief, the method takes advantage of the diffusion discrepancy $D_u \ll D_v$ and considering the limit $D_u \to 0, D_v \to \infty$, the stability of the homogenous steady state can be probed with respect to a 'local' perturbation in the form of a narrow peak of u with a negligible total mass, at some location in the domain. In this limit, the localized peak of u (u_L) does not influence the surrounding background u levels (u_G), whereas due to the 'infinitely fast' diffusion, v can be described by a single global variable (v_G) that is approximately uniformly distributed in space. This allows writing a set of ODEs that describe the evolution of the perturbation peak as:

$$\frac{\partial u_L}{\partial t} = f(u_L, c - u_G)$$

$$\frac{\partial u_G}{\partial t} = f(u_G, c - u_G) \qquad \text{(Eqs.2)}$$

Dynamics of this ODE system (Eqs.2) under variation of the total concentration c was explored using the Xppaut bifurcation software to produce Figure 7D. $f(u, v) = (k_0 + p \cdot k_1 \cdot u^2)v - k_2 \cdot u$, with the basal association/dissociation rate constants $k_0 = 0.2, k_2 = 0.1$, and a second-order self-amplification mechanism with rate constant $p \cdot k_1 = 0.4$. When external signal source is applied, k_1 is kept fixed and p is proportional to the signal strength (p>1). Symmetry breaking was observed for a broad range of parameters that sometimes occurred via a pitchfork bifurcation (for e.g., when $k_0 = 0.067, k_2 = 5, p \cdot k_1 = 20$).

The RD simulations of Eqs.1 (Figure 7E) were performed in 1D using a custom-made Python code, with $D_u = 0.01, D_v = 40$ and $c = 2000$. The integration time was set to 10^8, the time step – 10^{-6}, for a total of 10^3 spatial bins with step size 0.1, and periodic boundary conditions. To model the influence of an external signal gradient that imposes a template on a system with intrinsic self-organizing capabilities (Eqs. 1), we implemented a signaling source using a Gaussian distribution ($\mu = 50$, $\sigma_1 = 10$) with an amplitude scaled to 2.7.

Monte Carlo simulations of MT-membrane interactions

To simulate an array of MTs, we implemented an agent-based model that captures individual MT-dynamics (Dogterom and Leibler, 1993) together with stigmergic mechanism of local self-amplified membrane deformations formed by the interactions of MT-bundles with the membrane. A defined number of MTs are nucleated and evolve from fixed initial positions, mimicking a growth from a MT-organizing center. This initial MT–distribution reflects a radial MT distribution in the GUV in the interval $[0, \pi]$, and the distance of the membrane is set to 20 μm, approximating an average GUV radius. In brief, similarly as in (Cassimeris et al., 2018) we

assume that, rule 1: MTs are straight elements composed of a linear chain of subunits representing the length of the MT without incorporating molecular details; Rule 2: MT growth rate is linearly dependent on the free tubulin concentration; Rule 3: Tubulins released upon catastrophe events are immediately competent to polymerize without delay. According to Figure S1A, rule 4: the MT catastrophe rate k_c nonlinearly decreases with increase in tubulin concentration. The concentration of total tubulin was set to [Tub] = 30 μM, and the number of nucleation sites was set to 40, which also determines the maximum number of MTs. Additionally, we also assumed that, rule 5: Complete MT depolymerization immediately opens up that nucleation site for a new nucleation event. When a MT reaches the membrane, we assume that it pushes against it and generates local deformations. At this point, the following rules are implemented – Rule 6: We assume that the membrane exerts an elastic force on the MT proportional to the length of the protrusion $(F_e \sim c_1 \cdot \Delta h)$ that effectively slows down the growth velocity $(v_g \sim c_2 \cdot [\mathrm{Tub}] \cdot e^{-F_e/c_3})$ and thereby increases the catastrophe rate k_c:

$$k_c \sim \frac{c_4}{1+({}^{v_g}/_{v_0})} \quad \text{(Eq.3)}$$

The membrane curvature caused by the membrane deformation can capture free MTs, thereby generating a stigmergic effect in which MT-bundles are self-amplified and the deformations are stabilized (Figure 7D). Rule 7: we assume that each protruding MT will attract free neighboring radial MTs at a distance that scales with the length of the protrusion with an intensity of attraction $(I_a \sim \frac{\Delta h}{h}(1 - \frac{x}{\sigma(\Delta h)}))$. This dependency was derived from generic stigmergic models (Susnea and Axenie, 2015), where σ is the size of the attracting neighborhood corresponding to the size of the membrane deformation, x - position of the free radial MT to the deformation source, Δh - the extent of the deformation and h - the total MT length. Rule 8: free radial MTs that are initially positioned in two overlapping neighborhoods will be assigned to the deformation with a higher I_a. Keeping the position of the deforming MT fixed, the positioning of the free radial MTs is thereby updated to mimic formation of a MT-bundle. Rule 9: formed MT-bundles can also attract a MT-bundle that is localized in the attracting neighborhood if they have a higher intensity of attraction. Python-generated plot that depicts one realization of the evolution of the system from initially free radial MT distributions to stable MT-bundle distributions and the corresponding video was recorded and shown in Figure S1G and Video S2. We mainly observed end distributions of 3 or 4 stable MT-bundles for different initial radial MT distributions.

In the algorithm and correspondingly Video S2, the bundling is mimicked by overlaying the positioning of the attracted MTs to the position of the MT-bundle, and thereby the thickness of the lines does not represent the number of MTs in a bundle. The respective thickness of the MT-bundles is depicted only in Figures S1G and S1H where the individual MTs constituting a particular bundle are shown.

It was experimentally observed that under de-centering of the centrosome, more MTs approach the membrane at acute angle, leading to their buckling and gliding along the membrane. To simulate this situation in which buckling leads to gliding, we assumed that the centrosome lies on one of the foci of an ellipse, and thereby the free astral MTs that reach the membrane in the area enclosed with [semi-latus rectum, semi-major axis - linear eccentricity] as well as [semi-major axis, semi-major axis+linear eccentricity] will immediately glide and form two stable MT-bundles that deform the membrane at the opposite poles of the ellipse. This was implemented as

before, by keeping the position of the deforming MT fixed, and updating the positioning of the free radial MTs in the defined areas, thus forming these two MT-bundles. On the other hand, the MTs that reach the membrane between these intervals in the simulations are allowed to protrude the membrane, however they are not a source of attraction and thereby cannot form stable MT-bundles by themselves. In the simulation we observed that these free radial MTs will be eventually attracted to one of the pre-existing MT-bundles on the poles (Figure S1H; Video S2). The simulation parameters were taken as in (Cassimeris et al., 2018): $c_1 = \frac{0.5pN}{\mu m}, c_2 = 0.02\,{}^{\mu m}/_{s \cdot \mu M}, c_3 = 5pN, c_4 = 0.05s^{-1}, v_0 = 5.4\,{}^{\mu m}/_{s}$, total simulation time was set to N=1250 time steps. $\sigma(\Delta h)$ is proportional to the extent of the deformation with a scaling factor 1/11.

Reaction-diffusion simulation of gradients

We utilize numeric simulations of the reaction diffusion system to visualize the gradients resulting from localizing a kinase to the membrane of a GUV. Our kinetic measurements confirm two tubulin binding sites on stathmin. As the low affinity site (K_D = 2 µM for the unphosphorylated, > 200 µM for the phosphorylated state) has a high turnover rate, we consider a simplified setup of five "species": 1) free tubulin dimers and 2) free stathmin, 3) stathmin tubulin complex (in a 1:1 stoichiometry), 4) phosphorylated stathmin tubulin complex and 5) phosphorylated free stathmin. Here, species 2-5) are actually weakly associated with a second tubulin dimer that slows down effective diffusion, but whose binding state is not strongly influenced by phosphorylation. We assume that the pairwise association/dissociation and kinase/phosphatase reaction can be considered first-order processes governed by a back and a forth rate constant (equivalent to sub-saturation Michaelis-Menten-Kinetics) to reduce the number of parameters in the system. Considering a well-mixed volume (diffusion much faster than reaction), the balance of kinase/phosphatase reaction determines the steady-state levels of phosphorylated stathmin. For our measurements of k_{cat}/k_M (PPase 0.02 $\mu M^{-1}\ s^{-1}$; kinase 0.0011 $\mu M^{-1}\ s^{-1}$), at a stoichiometry of 1:1 about 5-10% of stathmin should be phosphorylated. By recruitment to the membrane, the concentration of the kinase is increased by a factor of up to 500. For this, a 5x increase of fluorescence intensity suffices, as the resolution of ~500 nm dilutes the signal of the "shell" of recruited kinase with a thickness of ~5 nm close to the membrane. Such recruitment would "invert" the phosphorylation and leave a fraction of <4% *un*phosphorylated stathmin at the membrane. If the phosphatase activity was also recruited, but to the center of the GUV, the result would be a linear gradient completely independent of diffusion, the amplitude of which would solely be determined by the relative strength of kinase and phosphatase activity. In such a case, diffusion would only change the amount of phosphorylated protein transported and how fast the gradient is established. However, as the soluble phosphatase is distributed evenly, the shape of the gradient arises from the interplay of diffusion, phosphatase activity and association/dissociation kinetics of stathmin-tubulin. As a further simplification, we disregarded the kinase activity in solution (much lower than phosphatase activity).

Reaction-diffusion simulations are performed by cellular automata approach (Schmick et al., 2014) 1D geometry, with a resolution of 0.01 µm per space unit. This corresponds to the kinase homogenously localized to the membrane of a spherical GUV. For a diffusion coefficient of 20 $\mu m^2\ s^{-1}$ of species 3+4), this translates to a diffusant radius of 3 space units and a time resolution of the simulation of 0.01 s per time step. The diffusant radius of species (1+2+5) is set to 4 space

units (corresponding to a slightly too high D = 35 $\mu m^2 s^{-1}$, avoiding numerical inconsistencies). Initial conditions were set for all association/dissociation of all species in steady-state without any kinase activity and setting kinase activity to its maximum instantaneously at t_0. Simulations continue until the relative change of the vectorial sum of all concentrations $<10^{-9}$ results in a steady-state distribution of all species. For dissociation/association reactions, the relevant rate constants are: $k_{on,stath} = 16\ s^{-1}$, $k_{off,stath} = 0.048\ s^{-1}$, $k_{on,p\text{-}stath} = 1.8\ s^{-1}$, $k_{off,p\text{-}stath} = 2.3\ s^{-1}$ and remain fixed across all simulations. In most experimental conditions, 2 – 5 μM of soluble kinase are used and we estimate the increase of concentration after translocation to the membrane by a factor of 200 – 500 to yield a kinase activity of $k_{kin} = 1\ s^{-1}$. Conversely, the phosphatase activity at 1 μM can be estimated as $k_{ppt} = 0.02\ s^{-1}$. These parameters produce a spatial distribution of the species (1-5) depicted in Figure S5E (left panel). Higher diffusivity of phospho-stathmin as compared to the tubulin-stathmin-complex (molecular weight 220 kDa, D = 20 $\mu m^2 s^{-1}$) leads to a depletion of the total stathmin (free, phosphorylated and tubulin-bound, cyan line in Figure S5E (left panel) at the membrane. This distribution is mirrored by the total tubulin due to its high association rate to stathmin.

Gradients of phosphorylated stathmin and free tubulin result from the competition of kinase activity that effectively "deposits" tubulin near the membrane and entropic redistribution by diffusion as well as rebinding to dephosphorylated unbound stathmin as driven by dephosphorylation. An activity of lambda phosphatase of 0.02 s^{-1} is sufficient to let the gradients decline within 1.5 μm distance from the membrane even at 10000 times faster kinase activity. Interestingly, varying the phosphatase activity for a kinase activity of 1 s^{-1} in agreement with our measurements shows an optimally steep gradient for 100 times slower phosphatase activity. Low phosphatase activity can saturate the GUV with phospho-stathmin and therefore free tubulin due to the shift in partitioning and yields a flat gradient with a high off-set. The highest phosphatase activity abolishes the phospho-stathmin gradient (zero amplitude and offset). Due to the association rate to (phospho-)stathmin being about 20 times faster than even kinase activity, the gradient of free tubulin is "locked" to the phospho-stathmin gradient (Figure 3C right panel; Figure S5E center).

DATA AND SOFTWARE AVAILABILITY

All custom-made code is available upon request to the corresponding author.

Video S1. Time-lapse of temperature-induced morphological state transitions corresponding to Figure 1C.

Video S2. Monte Carlo simulations of stigmergic membrane MT-aster interactions. Left: without forces on the centrosome, right: when centrosome decentering is considered. Corresponding to Figures S1G and S1H.

Video S3. 3D reconstruction of confocal z-stacks of Alexa488-SspB-AuroraB fluorescence (left: recruitment outside, right: recruitment inside) corresponding to Figure 2C.

Video S4. Time-lapse of Alexa647-tubulin (yellow) and Alexa488-SspB-AuroraB (magenta) at the equatorial plane of spherical SynMPS^{-stath} (left) and SynMPS (right) corresponding to Figure 4D.

Video S5. Time-lapse of Alexa647-tubulin (yellow, upper left), Alexa488-SspB-AuroraB (magenta, upper right), and transmission (lower left) at the equatorial plane of SynMPS corresponding to Figure 5B.

Video S6. 3D reconstruction of confocal z-stacks of Alexa647-tubulin fluorescence of SynMPS obtained before (left) and after (right) the time lapse series corresponding to Figure 5E.

Video S7. Time-lapse of Alexa647-tubulin (yellow, upper left), Alexa488-SspB-AuroraB (magenta, upper right), and transmission (lower left) at the equatorial plane of SynMPS corresponding to Figure 6A.

Video S8. 3D reconstruction of confocal z-stacks of Alexa647-tubulin fluorescence of SynMPS obtained before (left) and after (right) the time lapse series corresponding to Figure 6C.

Video S9. Time-lapse of Alexa647-tubulin (yellow, upper left), Alexa488-SspB-AuroraB (magenta, upper right), and transmission (lower left) at the equatorial plane of SynMPS corresponding to Figure 6D.

Video S10. 3D reconstruction of confocal z-stacks of Alexa647-tubulin fluorescence of SynMPS obtained before (left) and after (right) the time lapse series corresponding to Figure 6F.